AN EXPERIMENTAL AND ANALYTICAL STUDY OF PANTOGRAPH DYNAMICS

by

Steven Daniel Eppinger

Bachelor of Science
Massachusetts Institute of Technology
(February 1983)

SUBMITTED TO THE DEPARTMENT OF MECHANICAL ENGINEERING IN PARTIAL FULFILLMENT OF THE REQUIREMENTS FOR THE DEGREE OF

MASTER OF SCIENCE

at the

MASSACHUSETTS INSTITUTE OF TECHNOLOGY

May 1984

Signature of Author _____
Department of Mechanical Engineering
May 23, 1984

Certified by _____
Thesis Supervisor

Accepted by _____
Warren M. Rohsenow
Chairman, Department Thesis Committee

AN EXPERIMENTAL AND ANALYTICAL STUDY OF

PANTOGRAPH DYNAMICS

by

Steven Daniel Eppinger

Submitted to the Department of Mechanical Engineering on May 23, 1984 in partial fulfillment of the requirements for the degree of Master of Science.

Abstract

A study has been conducted of the performance of pantograph/catenary systems for electrified, high-speed rail vehicles. In this thesis, a general pantograph model is developed and augmented with specific elbow and suspension models which represent characteristics of a particular high-speed, intercity pantograph. The model is verified through dynamic tests conducted on the actual device, instrumented in the laboratory. A comparison confirms that the nonlinear model, with the proper choice of parameters, can accurately predict pantograph dynamics for frequencies past the pantograph's second modelled resonance. The model is to be used in computer simulations of pantograph/catenary interactions to study overall system performance under various conditions.

Thesis Supervisor: David N. Wormley
Title: Professor of Mechanical Engineering

Thesis Supervisor: Warren P. Seering
Title: Associate Professor of Mechanical Engineering

Acknowledgments

Over the course of a research project and during the production of a thesis, one receives the help of many friends and associates. Some of these supporters deserve special recognition.

This project was funded by the U.S. Department of Transportation, Office of University Research, under Grant Number DT-RS-56-81-C-00020. George Neat at the Transportation Systems Center provided the laboratory space for the experimental work. The technical assistance of Dan DeChristoforo, of T.S.C., has been greatly appreciated. Amtrak kindly loaned a pantograph for the testing. Mike Bitsura, of The Ringsdorff Corporation, advised in the setup and operation of the pantograph.

Professor Wormley has guided this project with foresight in research directions. Professor Seering's generous advice and encouragement allowed the rough spots to pass, eventually. His extra efforts have been deeply appreciated. Working with these two fine researchers has been an invaluable experience for me. Kurt Armbruster and Cal Vesely did the groundwork in the early model development, while Dave O'Connor later finished up the catenary work. Dave's help with the experiment and companionship throughout the project have been enjoyed. Gary Drlik assisted in the equation derivation and data processing.

Thanks are due to Bonnie Walters, of The Writing Program, who commented upon previous versions of this document. Weekly technical discussions with Pat Turner have helped me to gain the proper perspective on research issues. The kinship among the members of The Vehicle Dynamics Laboratory (Mike, Ademola, Gus, Long Chain, Dave, John, Dan, Mark, Kurt, Fort, Alex, Pat, Neal, Roberto, also "honorary members" -- Joan and Leslie) has aided in the completion of many Master's Theses.

Special thanks are owed to my family: to my parents, who showed me how to take a challenge; and to my wife, Julie, whose loving support made it possible.

Table of Contents

List of Figures

List of Tables

Chapter 1
Introduction

1.1 Background

Electrification of rail transport provides increased efficiency of power conversion over conventional fossil-fuel-based rail propulsion. Some diesel locomotives, for example, use internal combustion engines to generate power for the electric motors which turn the wheels. It is better, however, to generate electricity from petroleum on a much larger scale. Modern electric trains, therefore, use power generated at large plants and thus are more efficient and more reliable than their predecessors. The problem is then to pass the electricity to the train as it travels.

Usually, the power is transferred to the moving train by one of two simple means. The first lays a conducting member directly onto the rail bed, parallel to the two main rails. Current flows through this "third rail" and is collected by a pick-up roller on the train. This very reliable method is used for the shorter, intracity systems where access to the underground rail area is strictly limited.

The longer, intercity routes must use a more complex scheme, the pantograph/catenary system. The catenary is a structure of overhead current-carrying wires, suspended by supporting towers. A mechanical arm, known as a pantograph, is mounted atop the train and contacts the wire, passing the current to the train below. This scheme is favored for the longer installations

where safe access to the rail bed must be guaranteed.

1.2 Pantograph/Catenary Systems

Major sections of track have been electrified in both Europe and Japan, and more extensive conversions are planned. Pantograph/catenary systems are currently being used by the Japanese Shinkansen and Tokiado systems, the TGV and SNCF lines in France, and of course, in the United States along most of Amtrak's Northeast Corridor (Boston/New York/Washington). These rail systems have been extremely expensive to construct. Over half of their high capital cost can be charged to the construction of the overhead catenary system. Great interest has been expressed in understanding how to build less-expensive, better-performing systems and how to cheaply alter our present systems to more closely resemble the state-of-the-art.

Catenary Styles

The catenary is a compliant structure of wires which sags under its own weight and displaces upward with the contact force from the pantograph. The support towers are quite stiff and constrain the catenary displacement at the beginning and end of each span. Some typical catenary configurations are shown in Figure 1-1.

The simplest catenary, a single tensioned cable suspended between towers, is known as a trolley wire. The trolley wire, Figure 1-1a, is typically found in low-speed systems such as Boston's MBTA green-line.

The simple catenary, Figure 1-1b, provides more uniform compliance

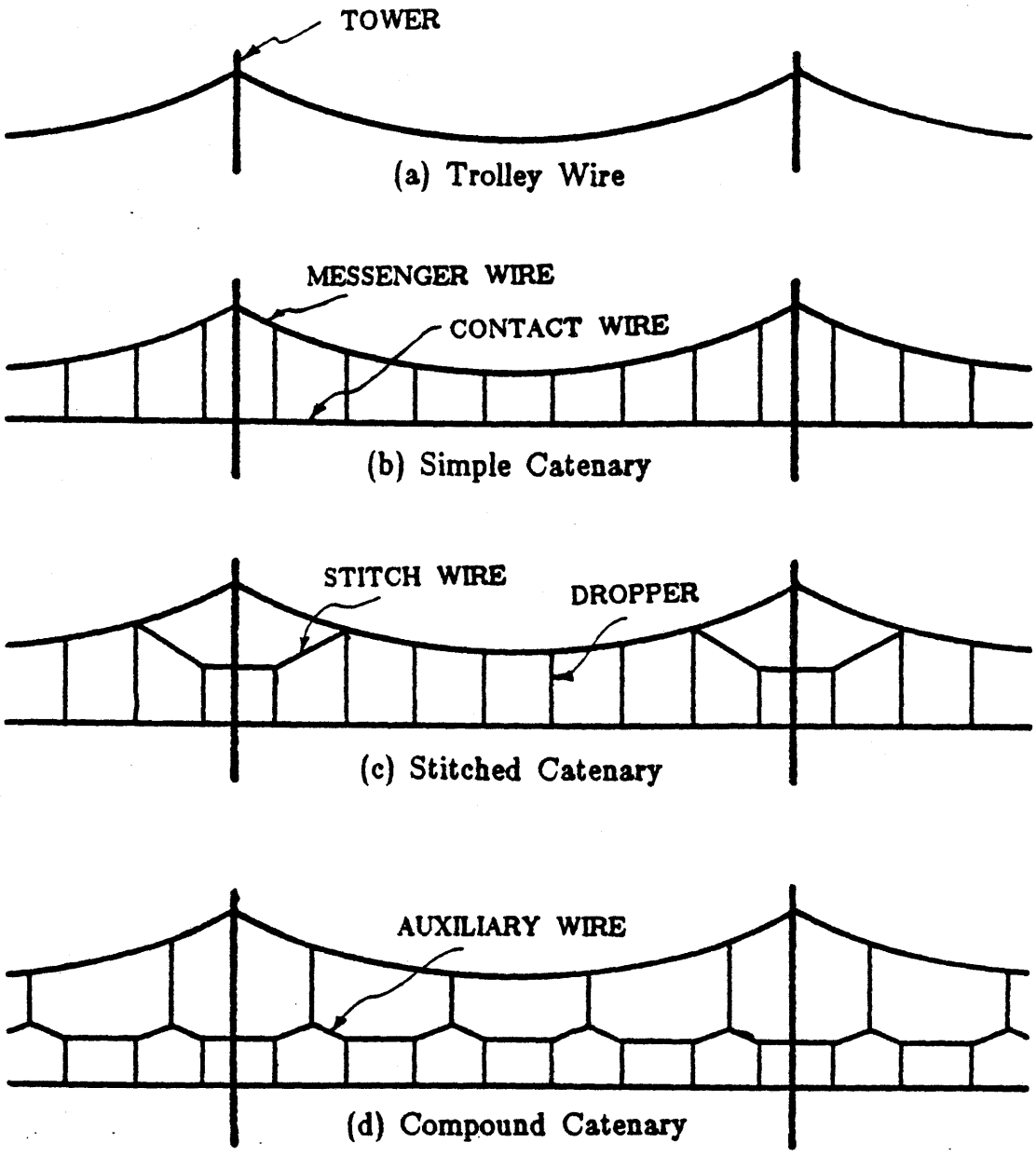

Figure 1-1: Common Catenary Configurations

along the length of a span. It consists of two tensioned wires. The upper, or messenger wire, is suspended between the towers and supports a number of droppers from which the contact wire hangs. In this configuration the catenary stiffness is still many times greater at the towers than elsewhere along the span.

The stitched catenary, Figure 1-1c, employs auxiliary wires which bypass the towers to gain more uniform stiffness. An even more complex design, the compound catenary, shown in Figure 1-1d, uses three tensioned wires with droppers to achieve the desired stiffness. All of the catenaries, however, have one common deficiency: they lack uniform compliance, so the pantograph cannot maintain a constant contact force as it travels along.

Pantograph Styles

There are many different pantograph designs. Figure 1-2 displays two common types. A simple pantograph might consist of a four-bar linkage designed to move the contacting shoe up and down in a nearly-straight line. Some sort of suspension, usually a spring or pneumatic cylinder, provides an uplift force. This single-stage pantograph is sketched in Figure 1-2a. The mass of the large frame necessary to span a broad range of operating heights can make the pantograph clumsy and unable to respond quickly to the changing catenary shape.

A dual-stage pantograph generally includes a large frame linkage similar to the single-stage pantograph and a relatively light and stiff head link designed to respond to the higher-frequency components of the catenary shape. Again, a suspension of some kind provides the uplift force. This pantograph

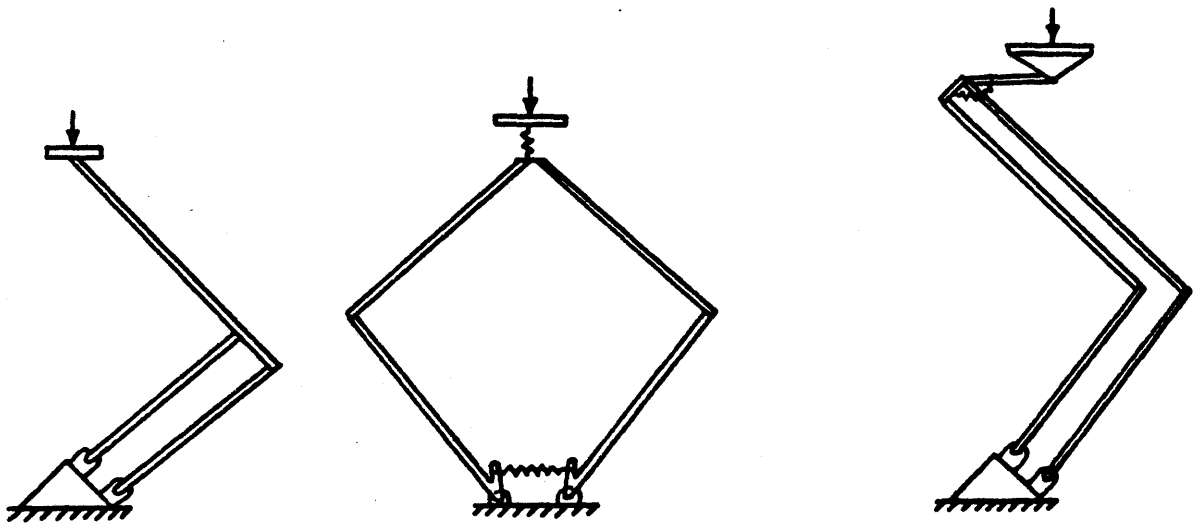

Figure 1-2: Common Pantograph Configurations

configuration is commonly found on long-distance, high-speed trains, while the simpler version typifies the slower, urban trolley systems. Figure 1-2b represents a dual-stage pantograph, the August-Stemman. It is of the symmetrical type, a five-bar linkage which requires a kinematic constraint to insure straight-line (vertical) motion. A light head with a stiff suspension are mounted above the symmetrical frame.

Figure 1-2c represents an asymmetrical dual-stage pantograph, such as the Faively or Brecknell-Willis models. The lower and upper frame arms can be considered four-bar linkages, and a head link supports the contacting shoe.

Dynamic Interaction

It is not the pantograph motion *per se* which gives rise to dynamic problems, but rather the interaction between the pantograph and catenary. Figure 1-3 shows a pantograph moving beneath a catenary.

The catenary displaces upward due to the contact force from the pantograph. In the center of a span, the catenary is "soft" and displaces a great deal. However, when the pantograph reaches a stiff tower, it is forced downward quite rapidly and tends to overshoot (downward) and may even lose contact. At this point, an electrical arc occurs as power to the train is interrupted. Some of the expensive catenary may be eroded away along with a bit of the pantograph's contacting shoe. Arcing can damage the engine's electric motors as well. Loss of contact is an important dynamic problem, and must be considered in pantograph design and analysis.

Ideally the pantograph should be able to:

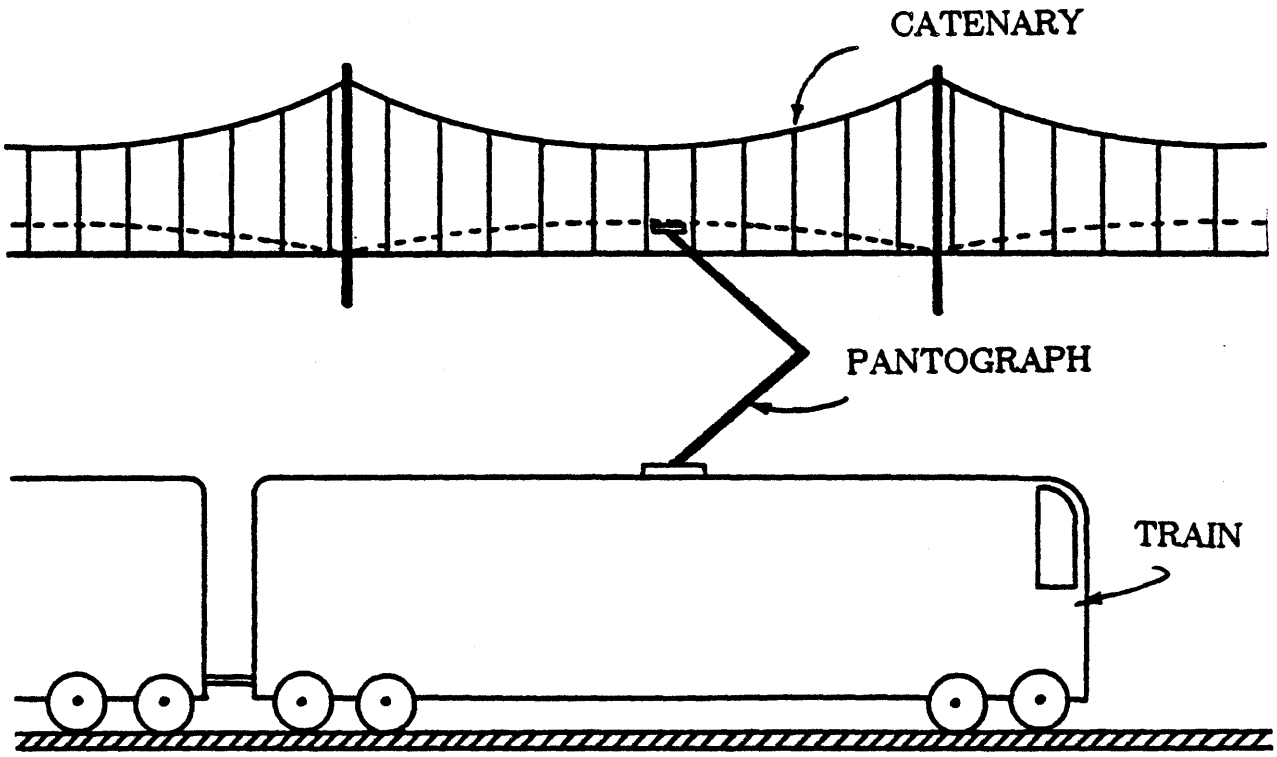

Figure 1-3: Pantograph/Catenary Interaction

- operate at a broad range of speeds and wire heights. (The catenary height may be low through tunnels and high in open areas.)
- operate with a minimum of contact force (to reduce wear of the catenary).
- *never* lose contact with the wire.

Since no pantograph posesses these characteristics, all are limited in operating speed.

1.3 Pantograph Modelling

In an effort to better understand the dynamic interaction of these systems, researchers have developed mathematical models which are used to predict performance. While the catenary models are generally quite complex, most pantograph models have been simple, lumped-mass representations.

Figure 1-4a shows a typical two-mass pantograph model. The system includes lumped masses for the pantograph frame and head, as well as suspensions between the two masses, and from the frame to ground. Simple nonlinearities, such as coulomb friction and nonlinear springs and dampers, can be easily added to this type of model. However, the lumped-mass representation does not model geometric nonlinearities of the frame, since the masses can only move vertically.

The geometrically nonlinear model of Figure 1-4b more closely depicts an actual pantograph. This type of model can be tailored to describe many different system configurations, also including coulomb friction, or nonlinear springs and dampers. A nonlinear model such as this is necessary to predict some of the special characteristics of the pantograph response.

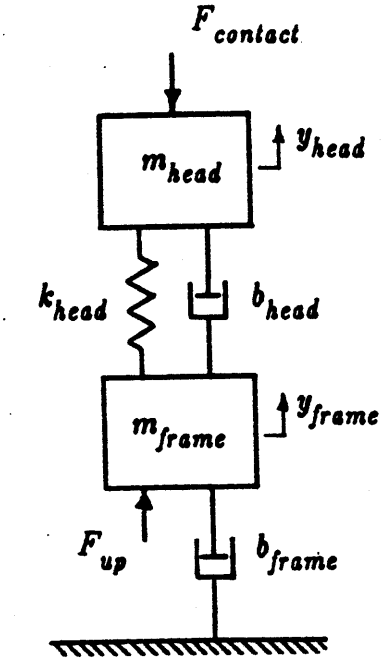

Linear, Two-Mass Model
(a)

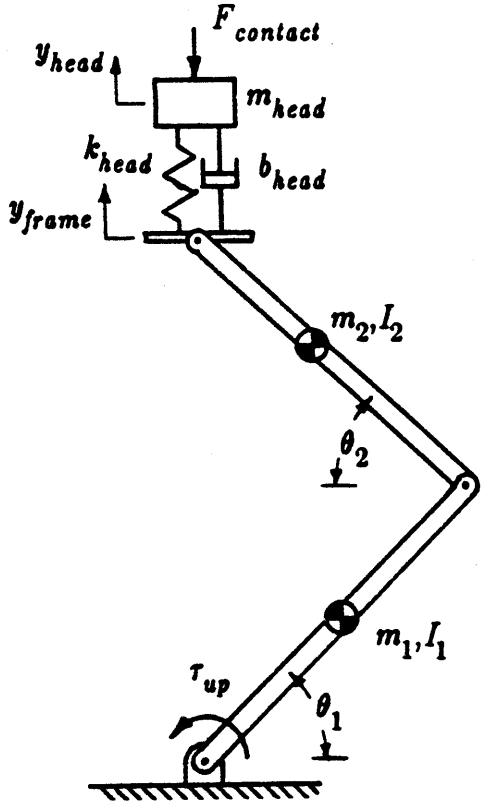

Geometrically Nonlinear Model
(b)

Figure 1-4: Pantograph Models

Many studies of pantograph/catenary system dynamics have been conducted using lumped-mass pantograph representations. This research investigates the use of a nonlinear model to better predict dynamic interaction.

1.4 Scope of Research

This research is part of a broader project, sponsored by the U.S. Department of Transportation, which aims to "understand pantograph/catenary systems in order to determine the design parameters which significantly affect their performance." The cost of a pantograph is quite small compared to that of the catenary system. If a better-performing pantograph could be developed for use with existing catenary systems in the U.S., an increase in operating speed could be achieved. In this project, both pantograph and catenary models have been developed to simulate dynamic interaction and study performance.

First, a modal catenary simulation was developed which is capable of predicting catenary response to a time-varying contact force input from a model pantograph. For the most part, a linear, two-mass pantograph model is used in simulating the dynamic interaction.

In parallel with the catenary work, a nonlinear pantograph model has been developed and tested. This model considers the geometric nonlinearities of the frame linkages, the coupling among the various links, and the nonlinear suspension characteristics as well.

The pantograph model has been verified by correctly predicting the dynamics of a Brecknell-Willis pantograph, which has been instrumented and tested in the laboratory. The nonlinear pantograph model is then used in

place of the two-mass pantograph model in conjunction with the catenary model to best predict the response of the coupled system. Finally, these models are used both separately and together in design parameter studies aimed at understanding the performance of various systems configurations.

This thesis presents the development and use of the nonlinear pantograph model and the associated experimental work. The next chapter reviews recent work in related areas. In Chapter Three, the pantograph model and simulation are developed. The following chapter discusses the laboratory testing of a high-speed pantograph. Chapter Five presents the results of the two studies and their correlation. The final chapter draws some conclusions from this project and makes recommendations concerning future research in the area.

Chapter 2
Literature Survey

In the past twenty-five years, much research has been conducted to understand and improve pantograph/catenary systems. Some of the more important pantograph studies are reviewed here, while many of the catenary works have been discussed by O'Connor [12] and Armbruster [1]. A more complete survey of the recent literature in these areas is included in the first annual report of this project [20].

Studies of Pantograph Dynamics

Research has concentrated on improving pantograph dynamics, since a better-performing pantograph makes possible the construction of less-expensive catenaries and allows higher-speed operation under existing catenaries. Many authors [4, 6, 7, 8, 11] suggest that reducing head mass is a key element in improving performance. A lighter head, with less inertia, is better able to track the high-frequency components of the wire shape. Gostling and Hobbs [11] support this recommendation, but further suggest that the head suspension be kept soft.

Belyaev, et al., [2] tested two Soviet pantographs and found that the lighter of them performed better at high speeds; however, the authors were concerned with its sturdiness. They also added viscous damping to the heads and found that this change resulted in a more uniform contact force history in both cases. Boissonnade [4] tested the Faiveley high-speed pantograph on the

French SNCF line. He advocates both the reduction of head mass and the increase of head damping on all pantographs. Further he suggests that "one-way" damping could decrease loss of contact. This nonlinear damper, resisting only the downward motion of the head, was not tested.

Peters [13] performed tests on both the single- and dual-stage Faiveley pantographs. He used loss-of-contact duration as the performance criterion. Peters reports that short separations, less than 5 ms, result in small, low-temperature, electric arcs that cause no damage to the pantograph head or contact wire. Separations of medium duration, 5 to 20 ms, are the most damaging to the catenary and contact shoe. For durations of greater than 20 ms, the forward motion of the train extinguishes the arc. This causes loss of power to the train, but no additional damage. Peters reports that significant improvements were observed by increasing the uplift force and reducing the head mass.

Recently, British rail's Research and Development Division and Brecknell-Willis & Co., Ltd. completed the development of the "BR-BW Highspeed Pantograph". Coxen et al., [8] report that this simple, high-performance pantograph allows train speeds to be increased significantly for given standards of contact loss. This asymmetrical pantograph features a light head link with a torsional spring suspension. Flow to a pneumatic cylinder, which provides the uplift force, passes through a small orifice, adding both stiffness and damping to the frame at high frequencies. Airfoils are used to overcome aerodynamic asymmetries.

At M.I.T., Vesely [17] developed a nonlinear dynamic pantograph model, describing the August-Stemman (symmetrical) pantograph. He performed frequency response tests in the laboratory to confirm that the model

predictions correlated well with the experimental data up to a 13 Hz excitation frequency, above which unmodelled structural effects became important. Vesely suggests that the two-mass model may be a suitable representation of the actual system for displacements less than 20 cm.

Several researchers have studied the use of active elements to improve pantograph performance. Wann [19] compared passive and several classically-controlled active designs. He showed that active elements have the potential to significantly improve pantograph performance. Sikorsky Aircraft [14] mounted hydraulic actuators to the frame of an August-Stemman pantograph. A suitable control system was not found. Belyaev, et al., [2] considered using an active pneumatic cylinder on a TS-IM pantograph to stabilize the contact force against the catenary. Vinayagalingam [18] simulated two active pantograph designs, a frame-actuated controller and his own "panhead inertia compensated" controller. Neither design showed any significant reduction in contact force variation.

Most of the pantograph models used are geometrically linear, lumped-mass models, such as the two-mass model shown in Figure 1-4. Both Coxen [8] and Vesely [17] developed nonlinear pantograph models which showed good agreement with the physical systems. The evolution of a more accurate, generic pantograph model should aid in the further development of pantograph/catenary systems.

This thesis presents the development of a general nonlinear pantograph model, which is augmented with specific elbow and cylinder models to describe the Brecknell-Willis pantograph. The model is verified through comparison with results from laboratory testing of the actual device.

Chapter 3
Analytical Models

Several dynamic models are developed in order to study pantograph performance. A nonlinear model, while fairly complex, is best able to predict the pantograph behavior. First the general pantograph model is discussed, and then the necessary elbow and cylinder models are developed to form a nonlinear model which describes the Brecknell-Willis pantograph.

The Brecknell-Willis pantograph is of the asymmetrical type described in Chapter 1. It consists of two frame arms which raise a head link to support the contacting shoe. This pantograph, designed for high-speed, intercity use, is sketched in Figure 3-1. The lower arm of the frame is actually a linkage designed to raise the upper arm with the lower. The upper arm, a simple four-bar linkage, provides a "datum" angle with respect to which the head link rotates. A pneumatic cylinder gives an uplift force to the frame. As air rushes in and out of the cylinder, it passes through a small orifice to add damping to the system. A sketch of the Brecknell-Willis pantograph configuration is shown in Figure 3-2.

3.1 General Pantograph Model

While the general pantograph model developed, with the proper choice of parameters, can represent many pantograph configurations, it is presented here to describe an asymmetrical pantograph such as the Brecknell-Willis. The

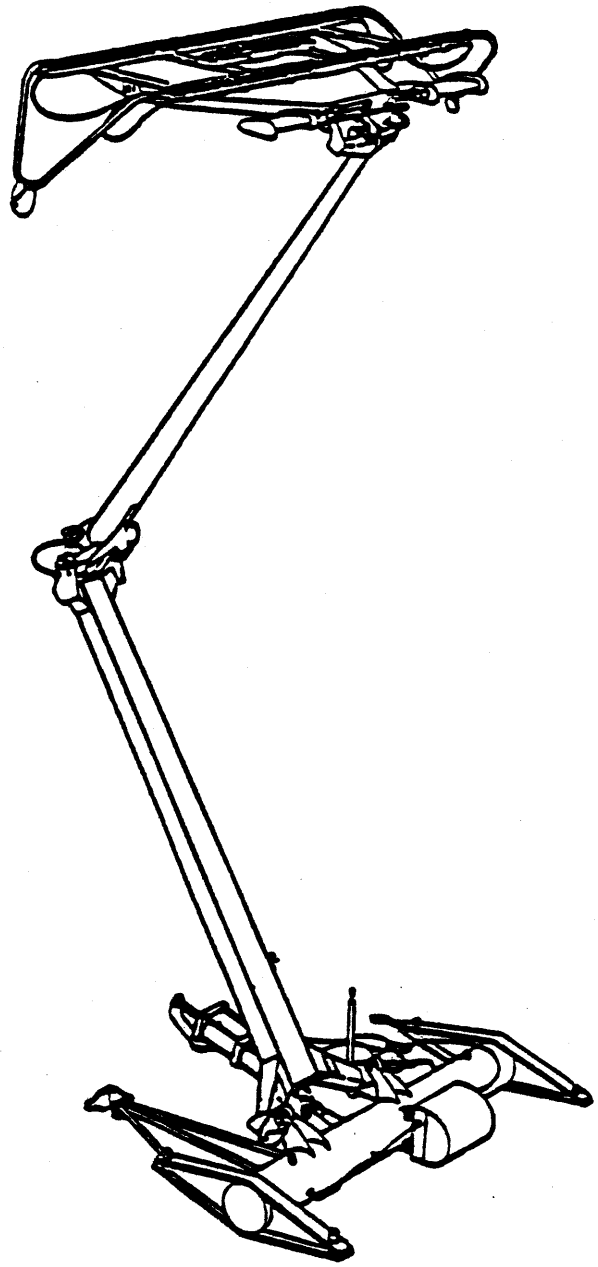

Figure 3-1: Brecknell-Willis Pantograph

Sketch Courtesy of the Ringsdorff Corporation

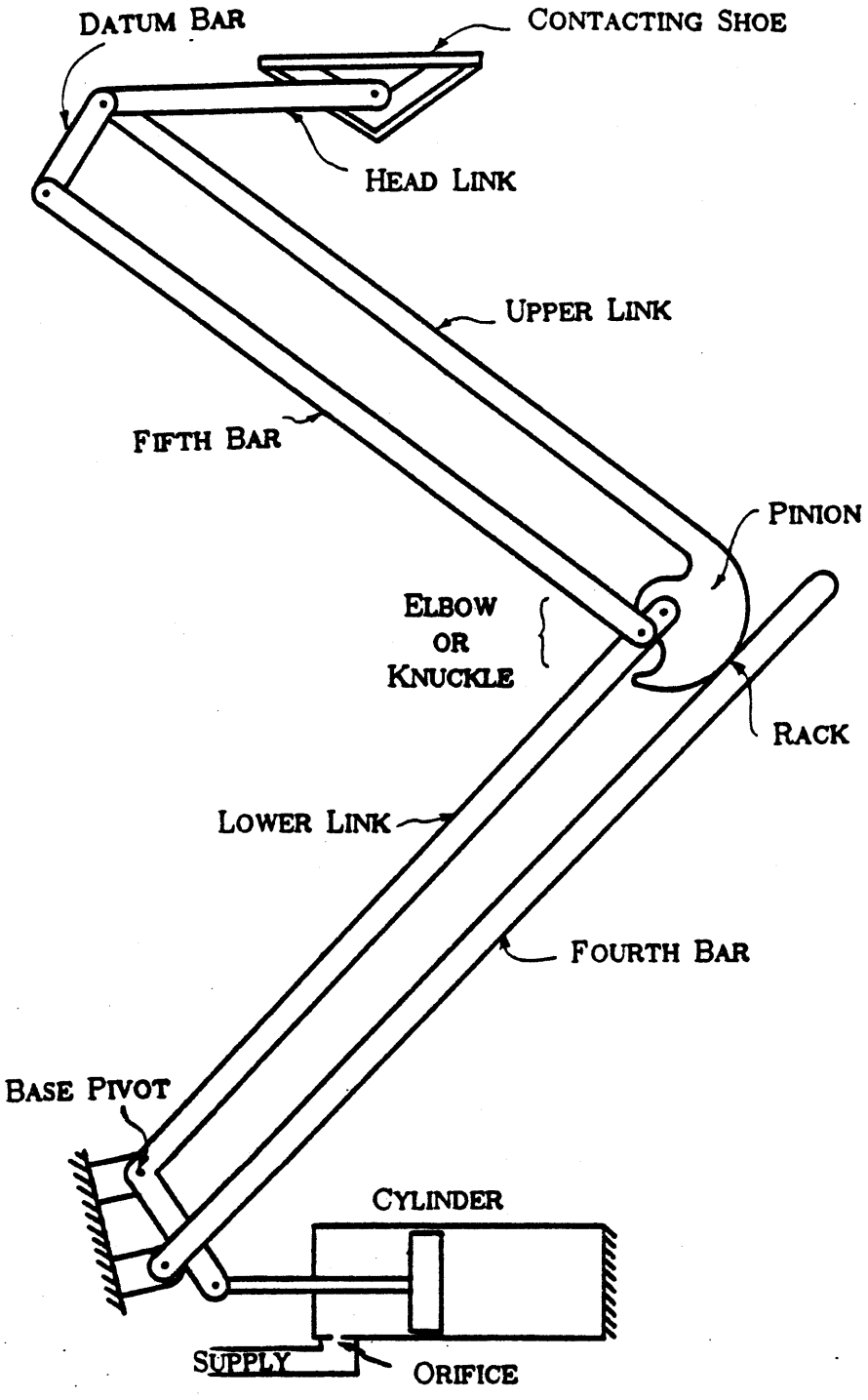

Figure 3-2: Brecknell-Willis Pantograph Mechanism

general pantograph model includes three degrees of freedom: lower frame link rotation, upper frame link rotation, and head link rotation. An elbow model is added to constrain the upper arm to raise with the lower. In addition, a frame suspension must provide an uplift force to the pantograph. Two suspension cylinder models are discussed.

Model Description

Figure 3-3 is a sketch of the nonlinear pantograph model developed. The three degrees of freedom are described by the generalized coordinates θ_1, θ_2, and θ_h for the rotations of the lower arm, upper arm, and head link respectively. All three angles are measured with respect to the horizontal and signed as shown. For this derivation, the frame linkages are considered to be rigid bodies.

The lower arm then has a length l_1, a lumped mass m_1, and a moment of intertia I_1 about the center of mass which lies at a distance d_1 from the base pivot. The upper arm has similar dimensions l_2 and d_2, and mass properties m_2 and I_2. The head link is described by the parameters l_h, d_h, m_h, and I_h, as shown.

The head spring constant, k_h, represents the stiffness of the torsional spring between the head link and the datum bar. The datum bar, for the derivation, is assumed to maintain a constant angle. One end of the head spring is therefore tied to ground as shown in Figure 3-3. The shoe stiffness parameter k_s describes the flexure of the contacting carbons and their supporting structure.

At each of the joints, both viscous damping and coulomb friction are

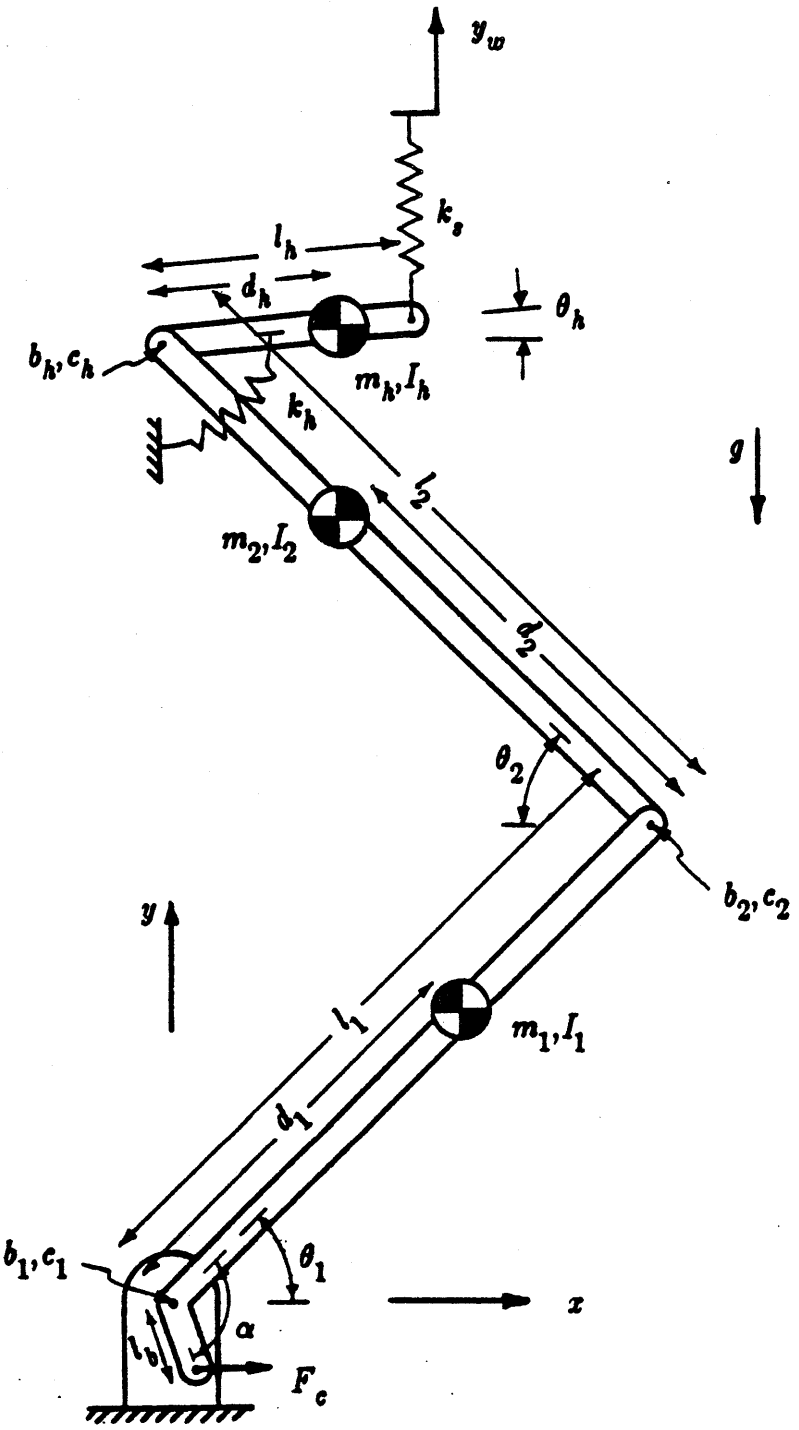

Figure 3-3: Nonlinear Pantograph Model

included. These parameters are assigned the values b_1, b_2, b_h, c_1, c_2, and c_h and are applied as shown in the sketch.

A displacement input y_w models the time-varying catenary height. The input force, F_c, from the pneumatic cylinder suspension is applied at a fixed angle α from the lower link and through a moment arm of length l_b as shown in the sketch. This input force, which may also vary with time, not only must overcome the weight of the links due to gravity but also must provide an uplift force against the wire.

The elbow and suspension models are discussed below in sections 3.2 and 3.3 respectively.

Equation Derivation

The governing equations for the nonlinear model described above are derived using Lagrange's (energy-based) method, discussed in [9]. While only a summary of the equation derivation is presented here, the details are given in Appendix A.

First the kinetic coenergy T^* is written as a sum of simple terms which account for the motions of the three links.

$$T^* = \tfrac{1}{2}(I_1+m_1 d_1^2)\dot{\theta}_1^2 + \tfrac{1}{2}I_2\dot{\theta}_2^2 + \tfrac{1}{2}m_2(\dot{x}_2^2+\dot{y}_2^2) + \tfrac{1}{2}I_h\dot{\theta}_h^2 + \tfrac{1}{2}m_h(\dot{x}_h^2+\dot{y}_h^2) \qquad (3.1)$$

The potential energy V is then written to include the effects of gravity and the two springs.

$$V = \tfrac{1}{2}k_h\theta_h^2 + \tfrac{1}{2}k_s(y_w-y_d)^2 + m_1 g y_1 + m_2 g y_2 + m_h g y_h \qquad (3.2)$$

The two energy terms must then be expressed as functions of only the state variables θ_1, θ_2, and θ_h. So we have

$$\begin{aligned}
T^* = {} & \tfrac{1}{2}[I_1+m_1 d_1^2]\dot{\theta}_1^2 + \tfrac{1}{2}I_2\dot{\theta}_2^2 + \tfrac{1}{2}I_h\dot{\theta}_h^2 \\
& + \tfrac{1}{2}m_2[l_1^2\sin^2\theta_1\dot{\theta}_1^2 + d_2^2\sin^2\theta_2\dot{\theta}_2^2 - 2l_1 d_2\sin\theta_1\sin\theta_2\dot{\theta}_1\dot{\theta}_2 \\
& \qquad + l_1^2\cos^2\theta_1\dot{\theta}_1^2 + d_2^2\cos^2\theta_2\dot{\theta}_2^2 + 2l_1 d_2\cos\theta_1\cos\theta_2\dot{\theta}_1\dot{\theta}_2] \\
& + \tfrac{1}{2}m_h[l_1^2\sin^2\theta_1\dot{\theta}_1^2 + l_2^2\sin^2\theta_2\dot{\theta}_2^2 + d_h^2\sin^2\theta_h\dot{\theta}_h^2 \\
& \qquad - 2l_1 l_2\sin\theta_1\sin\theta_2\dot{\theta}_1\dot{\theta}_2 + 2l_1 d_h\sin\theta_1\sin\theta_h\dot{\theta}_1\dot{\theta}_h \\
& \qquad - 2l_2 d_h\sin\theta_2\sin\theta_h\dot{\theta}_2\dot{\theta}_h \\
& \qquad + l_1^2\cos^2\theta_1\dot{\theta}_1^2 + l_2^2\cos^2\theta_2\dot{\theta}_2^2 + d_h^2\cos^2\theta_h\dot{\theta}_h^2 \\
& \qquad + 2l_1 l_2\cos\theta_1\cos\theta_2\dot{\theta}_1\dot{\theta}_2 + 2l_1 d_h\cos\theta_1\cos\theta_h\dot{\theta}_1\dot{\theta}_h \\
& \qquad + 2l_2 d_h\cos\theta_2\cos\theta_h\dot{\theta}_2\dot{\theta}_h]
\end{aligned} \tag{3.3}$$

and

$$\begin{aligned}
V = {} & \tfrac{1}{2}k_h\theta_h^2 \\
& + \tfrac{1}{2}k_s[y_w^2 + l_1^2\sin\theta_1^2 + l_1^2\sin\theta_2^2 + l_h^2\sin\theta_h^2 \\
& \qquad - 2y_w l_1\sin\theta_1 - 2y_w l_2\sin\theta_2 - 2y_w l_h\sin\theta_h \\
& \qquad + 2l_1 l_2\sin\theta_1\sin\theta_2 + 2l_1 l_h\sin\theta_1\sin\theta_h + 2l_2 l_h\sin\theta_2\sin\theta_h] \\
& + m_1 g d_1\sin\theta_1 + m_2 g(l_1\sin\theta_1 + d_2\sin\theta_2) \\
& + m_h g(l_1\sin\theta_1 + l_2\sin\theta_2 + d_h\sin\theta_h).
\end{aligned} \tag{3.4}$$

The work done by all of the non-conservative forces is summed to account for the viscous damping, coulomb friction, and input force. Then

$$\sum F_{nc}\cdot\delta r_{nc} = \sum \Xi_i\delta\theta_i \qquad \text{for } i = 1,\ 2,\ \text{and } h \tag{3.5}$$

and we find the three external torques to be

$$\Xi_1 = F_c l_b \sin(\alpha-\theta_1) - b_1\dot{\theta}_1 - b_2(\dot{\theta}_1+\dot{\theta}_2) - c_1\mathrm{sgn}(\dot{\theta}_1) - c_2\mathrm{sgn}(\dot{\theta}_1+\dot{\theta}_2) \tag{3.6}$$

$$\Xi_2 = -b_2(\dot{\theta}_1+\dot{\theta}_2) - b_h(\dot{\theta}_2+\dot{\theta}_h) - c_2\mathrm{sgn}(\dot{\theta}_1+\dot{\theta}_2) - c_h\mathrm{sgn}(\dot{\theta}_2+\dot{\theta}_h) \tag{3.7}$$

$$\Xi_h = -b_h(\dot{\theta}_2+\dot{\theta}_h) - c_h\mathrm{sgn}(\dot{\theta}_2+\dot{\theta}_h). \tag{3.8}$$

Now we form the Lagrangian $\mathcal{L} = T^* - V$ and use Lagrange's equation

$$\frac{\mathrm{d}}{\mathrm{dt}}\left(\frac{\partial \mathcal{L}}{\partial \dot{\theta}_i}\right) - \left(\frac{\partial \mathcal{L}}{\partial \theta_i}\right) = \Xi_i \qquad \text{for } i = 1,\ 2,\ \text{and } h \tag{3.9}$$

to write the three governing equations.

These equations, which are taken from Appendix A, are coupled and must be solved simultaneously. For $i = 1$, the first governing equation is:

$$\begin{aligned}
&\ddot{\theta}_1[I_1 + m_1 d_1^2 + m_2 l_1^2 + m_h l_1^2] \\
&+ \ddot{\theta}_2[(m_2 l_1 d_2 + m_h l_1 l_2)\cos(\theta_1+\theta_2)] \\
&+ \ddot{\theta}_h[m_h l_1 d_h \cos(\theta_1-\theta_h)] \\
&= \dot{\theta}_2^2(m_2 l_1 d_2 + m_h l_1 l_2)\sin(\theta_1+\theta_2) \\
&+ \dot{\theta}_h^2(m_h l_1 d_h)\ \sin(\theta_h-\theta_1) \\
&+ \cos\theta_1(k_s y_w l_1 - m_1 g d_1 - m_2 g l_1 - m_h g l_1) \\
&- \sin\theta_1\cos\theta_1(k_s l_1^2) - \cos\theta_1\sin\theta_2(k_s l_1 l_2) - \cos\theta_1\sin\theta_h(k_s l_1 l_h) \\
&+ F_c l_b \sin(\alpha-\theta_1) - b_1\dot{\theta}_1 - b_2(\dot{\theta}_1+\dot{\theta}_2) \\
&- c_1\mathrm{sgn}(\dot{\theta}_1) - c_2\mathrm{sgn}(\dot{\theta}_1+\dot{\theta}_2).
\end{aligned} \tag{3.10}$$

For $i = 2$, the second governing equation is:

$$
\begin{aligned}
&\ddot{\theta}_1[(m_2 l_1 d_2 + m_h l_1 l_2)\cos(\theta_1+\theta_2)] \\
&+ \ddot{\theta}_2[I_2 + m_2 d_2^2 + m_h l_2^2] \\
&+ \ddot{\theta}_h[m_h l_2 d_h \cos(\theta_2+\theta_h)] \\
&= \dot{\theta}_1^2(m_2 l_1 d_2 + m_h l_1 l_2)\sin(\theta_1+\theta_2) \\
&+ \dot{\theta}_h^2(m_h l_2 d_h)\sin(\theta_2+\theta_h) \\
&+ \cos\theta_2(k_s y_w l_2 - m_2 g d_2 - m_h g l_2) \\
&- \sin\theta_2\cos\theta_2(k_s l_2^2) - \sin\theta_1\cos\theta_2(k_s l_1 l_2) - \cos\theta_2\sin\theta_h(k_s l_2 l_h) \\
&- b_2(\dot{\theta}_1+\dot{\theta}_2) - b_h(\dot{\theta}_2+\dot{\theta}_h) - c_2\,\mathrm{sgn}(\dot{\theta}_1+\dot{\theta}_2) - c_h\,\mathrm{sgn}(\dot{\theta}_2+\dot{\theta}_h).
\end{aligned}
\tag{3.11}
$$

For $i = h$, the third governing equation is:

$$
\begin{aligned}
&\ddot{\theta}_1[m_h l_1 d_h \cos(\theta_1-\theta_h)] \\
&+ \ddot{\theta}_2[m_h l_2 d_h \cos(\theta_2+\theta_h)] \\
&+ \ddot{\theta}_h[I_h + m_h d_h^2] \\
&= \dot{\theta}_1^2(m_h l_1 d_h)\sin(\theta_1-\theta_h) \\
&+ \dot{\theta}_2^2(m_h l_2 d_h)\sin(\theta_2+\theta_h) \\
&+ \cos\theta_h(k_s y_w l_h - m_h g d_h) - \sin\theta_h\cos\theta_h(k_s l_h^2) \\
&- \sin\theta_1\cos\theta_h(k_s l_1 l_h) - \sin\theta_2\cos\theta_h(k_s l_2 l_h) \\
&- \theta_h k_h - b_h(\dot{\theta}_2+\dot{\theta}_h) - c_h\,\mathrm{sgn}(\dot{\theta}_2+\dot{\theta}_h).
\end{aligned}
\tag{3.12}
$$

3.2 Elbow Model

In order to provide that the upper arm generally rises with the lower, the actual linkage sketched in Figure 3-4a must be considered. The lower arm mechanism consists of two long links pinned a fixed distance apart at their base ends. At the elbow ends of these links are a rack and pinion. (This arrangement more closely resembles a sprocket and chain.) The upper arm is attached to the pinion.

This elbow, however, is not infinitely stiff. While θ_2 increases with θ_1 for the slow motion of the pantograph, at higher excitation frequencies, the angular velocities $\dot{\theta}_1$ and $\dot{\theta}_2$ may be of opposite sign. An elbow model must be included to establish static and dynamic properties of θ_2.

An elbow link, with angle θ_e measured with respect to the horizontal as shown, represents the part of the elbow which moves with the lower arm. A torsional spring and damper are placed between this elbow link and an extension of the upper arm. The elbow is modelled as shown in Figure 3-4b. The parameters k_e and b_e are chosen to represent the torsional stiffness and viscous damping of the transmission at the elbow. The kinematic relation between θ_e and θ_1 is derived for the true configuration of Figure 3-4a instead of the four-bar linkage sketched.

To incorporate this elbow model into the general pantograph model, we must add the potential energy term

$$\Delta V = \tfrac{1}{2}k_e(\theta_e - \theta_2)^2 \tag{3.13}$$

and the non-conservative work term

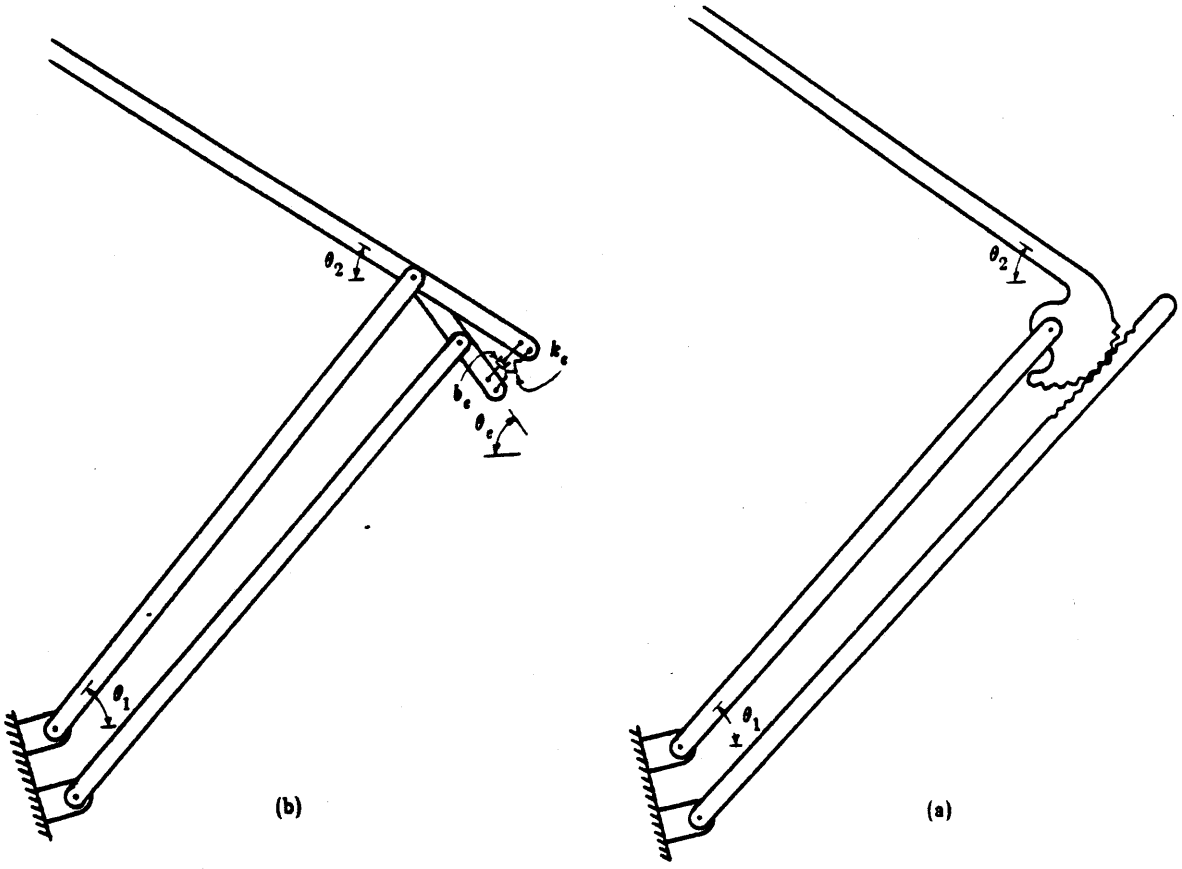

Figure 3-4: Brecknell-Willis Elbow Model

$$\sum F_{nc} \cdot \delta r_{nc} = -b_e(\dot{\theta}_e - \dot{\theta}_2)(\delta\theta_e - \delta\theta_2). \tag{3.14}$$

Of course, we do not change the kinetic coenergy term T^* since no mass or inertia has been added.

Now θ_e and $\dot{\theta}_e$ must be expressed as functions of the state variables θ_1 and $\dot{\theta}_1$. We will also need $\frac{\delta\theta_e}{\delta\theta_1}$ as a function of θ_1. These kinematic relations are derived in Appendix B, although not in closed form. For the governing equations, we will continue to use the symbols, θ_e, $\dot{\theta}_e$, and $\frac{\delta\theta_e}{\delta\theta_1}$ as necessary.

Using Lagrange's equation, Equation (3.9), we simply add the two torque terms $k_e(\theta_e - \theta_2)\frac{\delta\theta_e}{\delta\theta_1}$ and $-b_e(\dot{\theta}_e - \dot{\theta}_2)\frac{\delta\theta_e}{\delta\theta_1}$ to the left- and right-hand sides of Equation (3.10) respectively. Also we add the terms $k_e(\theta_2 - \theta_e)$ and $-b_e(\dot{\theta}_e - \dot{\theta}_2)$ to the left- and right-hand sides of Equation (3.11).

3.3 Cylinder Models

Two different models for the pneumatic suspension were developed. The nonlinear cylinder model Figure 3-5, considers the air to be an ideal gas which compresses reversibly. The flow is resisted as it passes through the small orifice to or from the constant supply pressure. The linear cylinder model, Figure 3-6, treats the compressible fluid as a simple spring and the orifice as a viscous damper in series.

Either cylinder model adds a new state variable, P, to the list of generalized coordinates used in the pantograph model. Therefore, for each case, we must derive a differential equation for the new state of the form $\dot{P} = f(\theta_1, \dot{\theta}_1, P)$ and then couple the two systems by defining the input force $F_c = f(\theta_1, P)$.

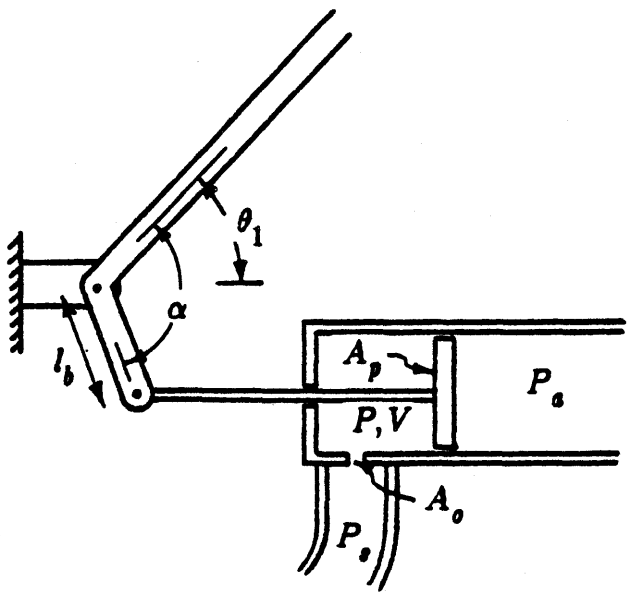

Figure 3-5: Nonlinear Cylinder Model

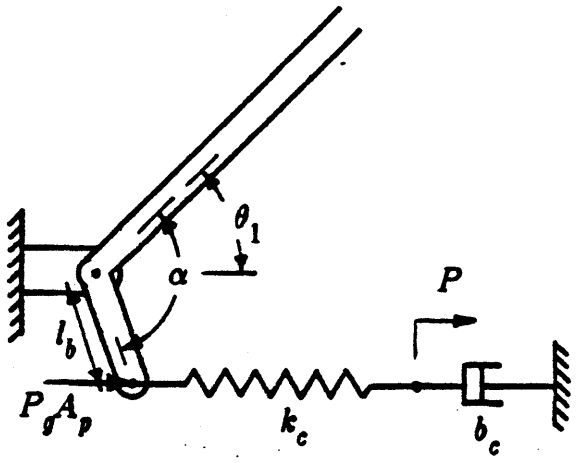

Figure 3-6: Linear Cylinder Model

Nonlinear Cylinder Model Development

In this model, the new state variable, P, is simply the pressure of the air inside the pneumatic cylinder.

We assume the air in the cylinder to be an ideal gas. The mass of that air is then given by the perfect gas law,

$$m = \frac{PV}{RT} . \tag{3.15}$$

where P, V, and T are the cylinder pressure, volume, and temperature respectively, and R is the universal gas constant. We assume that the process is sufficiently slow to maintain a constant gas temperature. Then differentiating equation (3.15) with respect to time in order to find the mass flow rate with T constant, we have

$$\dot{m} = \frac{dm}{dt} = \frac{P}{RT}\frac{dV}{dt} + \frac{V}{RT}\frac{dP}{dt} . \tag{3.16}$$

The flow rate through the small orifice is a function of the upstream and downstream pressures. This relation for compressible flow through an orifice is given by reference [3] as follows:

$$\dot{m} = c_d A_o \sqrt{\frac{2\gamma}{R(\gamma-1)}} \frac{P_u}{\sqrt{T}} \left(\frac{P_d}{P_u}\right)^{\frac{1}{\gamma}} \sqrt{1 - \left(\frac{P_d}{P_u}\right)^{\frac{\gamma-1}{\gamma}}} \tag{3.17}$$

$$\text{for } .528 < \frac{P_d}{P_u} \leq 1.0$$

where c_d = discharge coefficient of the orifice

A_o = orifice area

γ = ratio of specific heats for the gas

P_u = upstream pressure

P_d = downstream pressure.

Equating the mass flow rates through the orifice and into the cylinder, we eliminate $\dot{m}$ and have the differential equation for the pressure.

$$\frac{dP}{dt} = \frac{RTc_d A_o}{V}\sqrt{\frac{2\gamma}{R(\gamma-1)}}\frac{P_u}{\sqrt{T}}\left(\frac{P_d}{P_u}\right)^{\frac{1}{\gamma}}\sqrt{1-\left(\frac{P_d}{P_u}\right)^{\frac{\gamma-1}{\gamma}}} - \frac{P}{V}\frac{dV}{dt} \tag{3.18}$$

where $P_d = P$ and $P_u = P_s$ for $P \leq P_s$

and $P_d = P_s$ and $P_u = P$ for $P > P_s$.

To implement this cylinder model, the differential equation for the pressure is integrated along with the governing equations for the pantograph. To couple the differential equations, we solve for the cylinder volume as a function of the lower frame link position, θ_1, and substitute into Equation (3.18)

$$V = V^o + A_p l_b \cos(\alpha-\theta_1) \tag{3.19}$$

and

$$\frac{dV}{dt} = A_p \dot{\theta}_1 \sin(\alpha-\theta_1) \tag{3.20}$$

where V^o is the cylinder volume when $(\alpha-\theta_1)=\frac{1}{2}\pi$ and A_p is the piston surface area. Now we have

$$\dot{P} = \frac{RTc_d A_o}{V^o + A_p l_b \cos(\alpha-\theta_1)}\sqrt{\frac{2\gamma}{R(\gamma-1)}}\frac{P_u}{\sqrt{T}}\left(\frac{P_d}{P_u}\right)^{\frac{1}{\gamma}}\sqrt{1-\left(\frac{P_d}{P_u}\right)^{\frac{\gamma-1}{\gamma}}}$$

$$- \frac{PA_p\dot{\theta}_1\sin(\alpha-\theta_1)}{V^o+A_p l_b\cos(\alpha-\theta_1)} . \tag{3.21}$$

Finally, to couple the cylinder force to the pantograph, we substitute into the first pantograph differential equation

$$F_c = (P - P_a)A_p \tag{3.22}$$

where P_a is the atmospheric pressure. Note that under static conditions, $\dot{\theta}_1=0$ and for $\dot{P}$ to be zero, $P_d=P_u$, so the pressure, P, must equal the absolute supply pressure, P_s. So

$$F_{static} = (P_s-P_a)A_p. \tag{3.23}$$

Linear Cylinder Model Development

In the linear model, the new state is the displacement P of the point between the spring and damper, as shown in Figure 3-6.

The differential equation governing the motion of P can be obtained by summing the two forces which act on the point.

$$k_c[P - l_b\cos(\alpha-\theta_1)] + b_c\dot{P} = 0. \tag{3.24}$$

Now, solving for $\dot{P}$

$$\dot{P} = \frac{k_c}{b_c}[l_b\cos(\alpha-\theta_1) - P]. \tag{3.25}$$

The force applied to the lower link is found by adding the spring tension to the external force

$$F_c = P_g A_p + k_c[P - l_b\cos(\alpha-\theta_1)] \tag{3.26}$$

where P_g is the supply gage pressure, $P_g=P_s-P_a$.

To implement this linear cylinder model, the differential equation for the motion of the point P, Equation (3.25), is integrated along with the governing equations of the pantograph. To couple the cylinder model to the pantograph, we substitute the input force given by Equation (3.26) into the first pantograph equation. Note that under static conditions, the force applied to the lower link is

$$F_{static} = P_g A_p \tag{3.27}$$

as in the nonlinear case.

3.4 Solution Technique

The governing equations for the general pantograph model are a set of three coupled, second-order differential equations. Before integrating, the second derivative terms are decoupled by their simultaneous solution.

We first write Equations (3.10), (3.11), and (3.12) in a convenient form.

$$\begin{aligned} A\ddot{\theta}_1 + B\ddot{\theta}_2 + C\ddot{\theta}_h &= D \\ E\ddot{\theta}_1 + F\ddot{\theta}_2 + G\ddot{\theta}_h &= H \\ I\ddot{\theta}_1 + J\ddot{\theta}_2 + K\ddot{\theta}_h &= L \end{aligned} \tag{3.28}$$

where

$$A = I_1 + m_1 d_1^2 + m_2 l_1^2 + m_h l_1^2$$

$$B = (m_2 l_1 d_2 + m_h l_1 l_2)\cos(\theta_1+\theta_2)$$

$$C = m_h l_1 d_h \cos(\theta_1-\theta_h)$$

$$\begin{aligned} D = {} & \dot{\theta}_2^2(m_2 l_1 d_2 + m_h l_1 l_2)\sin(\theta_1+\theta_2) \\ & + \dot{\theta}_h^2(m_h l_1 d_h)\ \sin(\theta_h-\theta_1) \\ & + \cos\theta_1(k_s y_w l_1 - m_1 g d_1 - m_2 g l_1 - m_h g l_1) \\ & - \sin\theta_1\cos\theta_1(k_s l_1^2) - \cos\theta_1\sin\theta_2(k_s l_1 l_2) - \cos\theta_1\sin\theta_h(k_s l_1 l_h) \\ & + F_c l_b \sin(\alpha-\theta_1) - b_1\dot{\theta}_1 - b_2(\dot{\theta}_1+\dot{\theta}_2) \\ & - c_1\mathrm{sgn}(\dot{\theta}_1) - c_2\mathrm{sgn}(\dot{\theta}_1+\dot{\theta}_2) \end{aligned}$$

$$E = (m_2 l_1 d_2 + m_h l_1 l_2)\cos(\theta_1+\theta_2)$$

$$F = I_2 + m_2 d_2^2 + m_h l_2^2]$$

$$G = m_h l_2 d_h \cos(\theta_2+\theta_h)$$

$$\begin{aligned} H = {} & \dot{\theta}_1^2(m_2 l_1 d_2 + m_h l_1 l_2)\sin(\theta_1+\theta_2) \\ & + \dot{\theta}_h^2(m_h l_2 d_h)\sin(\theta_2+\theta_h) \\ & + \cos\theta_2(k_s y_w l_2 - m_2 g d_2 - m_h g l_2) \\ & - \sin\theta_2\cos\theta_2(k_s l_2^2) - \sin\theta_1\cos\theta_2(k_s l_1 l_2) - \cos\theta_2\sin\theta_h(k_s l_2 l_h) \\ & - b_2(\dot{\theta}_1+\dot{\theta}_2) - b_h(\dot{\theta}_2+\dot{\theta}_h) - c_2\mathrm{sgn}(\dot{\theta}_1+\dot{\theta}_2) - c_h\mathrm{sgn}(\dot{\theta}_2+\dot{\theta}_h) \end{aligned}$$

$$I = m_h l_1 d_h \cos(\theta_1-\theta_h)$$

$$J = m_h l_2 d_h \cos(\theta_2+\theta_h)$$

$$K = I_h + m_h d_h^2$$

$$\begin{aligned} L = {} & \dot{\theta}_1^2(m_h l_1 d_h)\sin(\theta_1-\theta_h) \\ & + \dot{\theta}_2^2(m_h l_2 d_h)\sin(\theta_2+\theta_h) \end{aligned}$$

$$+ \cos\theta_h(k_s y_w l_h - m_h g d_h) - \sin\theta_h\cos\theta_h(k_s l_h^2)$$
$$- \sin\theta_1\cos\theta_h(k_s l_1 l_h) - \sin\theta_2\cos\theta_h(k_s l_2 l_h)$$
$$- \theta_h k_h - b_h(\dot{\theta}_2+\dot{\theta}_h) - c_h\mathrm{sgn}(\dot{\theta}_2+\dot{\theta}_h). \tag{3.29}$$

Using any suitable means (Cramer's rule, matrix inversion, or Gaussian elimination and back-substitution [16]), we can find decoupled expressions for the three accelerations.

$$\ddot{\theta}_1 = \frac{DFK + BGL + CHJ - LFC - HBK - DJG}{AFK + BGI + CEJ - IFC - EBK - AJG}$$
$$\ddot{\theta}_2 = \frac{AHK + DGI + CEL - IHC - EDK - ALG}{AFK + BGI + CEJ - IFC - EBK - AJG} \tag{3.30}$$
$$\ddot{\theta}_h = \frac{AFL + BHI + DEJ - IFD - EBL - AJH}{AFK + BGI + CEJ - IFC - EBK - AJG}$$

A numerical integration routine, based on the fourth-order Runge-Kutta method [15], is used to solve the differential equations for the time response. This integrator only works with first-order equations, so to the three acceleration equations, we add three (trivial) equations defining the velocity states. Finally, we choose one of the two cylinder equations and have seven first-order equations to determine the solution for the states θ_1, $\dot{\theta}_1$, θ_2, $\dot{\theta}_2$, θ_h, $\dot{\theta}_h$, and P.

The equations of motion are coded into a FORTRAN subroutine, EQSIM, included in Appendix C The software package DYSYS, used at M.I.T.'s Joint Computer Facility, provides the Runge-Kutta integrator and the necessary plotting routines.

3.5 Choice of Parameters

The many parameters for the nonlinear pantograph model, Figure 3-3, are listed in Table 3-I along with the values chosen to describe the Brecknell-Willis pantograph tested.

The physical dimensions l_1, l_2, and l_h representing the three link lengths were taken from the pantograph set up in the laboratory, and then verified with dimensions extracted from a set of assembly drawings, supplied by The Ringsdorff Corporation.

The masses m_1, m_2, and m_h, the moments of inertia I_1, I_2, and I_h, and the distances to link centers of mass d_1, d_2, and d_h, were estimated from known link properties.

The input spring constant, k_s, corresponds to the stiffness of the contacting shoe and its supporting structure. Its value was determined by removing the head, supporting it rigidly at the points where the apex frame attaches, and measuring both applied force and deflection of the carbons in a series of tests.

The head spring rate, k_h is a nonlinear function of the angle, θ_h. The spring includes the effects of the stop which limits the head rotation. The torques necessary to deflect the head link in both directions were recorded, along with the induced rotations.

The stop was found to be less than five times as stiff as the torsional spring designed to provide the stiffness k_h. Furthermore, the torsion bar is preloaded in such a way that for the small deflections of θ_h encountered in the laboratory testing, the head spring is always in the region governed by the

Table 3-I: Parameters for the Nonlinear Pantograph Model

variable	value	units	description
l_1	1.95	m	lower link length
l_2	1.95	m	upper link length
l_h	0.40	m	head link length
m_1	31.5	kg	lower link mass
m_2	25.2	kg	upper link mass
m_h	13.5	kg	head mass
I_1	11.7	kg-m^2	lower link moment of inertia
I_2	8.10	kg-m^2	upper link moment of inertia
I_h	0.432	kg-m^2	head moment of inertia
d_1	1.10	m	distance to lower link mass center
d_2	0.80	m	distance to upper link mass center
d_h	0.35	m	distance to head mass center
k_s	180000	N/m	input (catenary) spring constant
k_h	2250.0	N-m/rad	head spring constant
k_e	44640.0	N-m/rad	elbow stiffness
b_1	36.0	N-m-sec/rad	base viscous damping
b_2	157.5	N-m-sec/rad	knuckle viscous damping
b_h	10.8	N-m-sec/rad	head viscous damping
c_1	0.9	N-m	base coulomb friction
c_2	0.45	N-m	knuckle coulomb friction
c_h	0.45	N-m	head coulomb friction
x_f	0.120	m	x-coordinate of the base link
y_f	0.170	m	y-coordinate of the base link

Table 3-I, continued

l_e	0.082	m	length of the elbow link (pinion radius)
θ_e^o	-0.164	rad	initial value of θ_e (for θ_1=0)
l_b	0.235	m	moment arm length for cylinder
α	1.82	rad	angle between lower link and moment arm
A_p	0.0123	m^2	piston surface area
A_o	0.00000314	m^2	orifice area
V^o	0.000996	m^3	cylinder volume when $(\alpha-\theta_1)=\frac{1}{2}\pi$
P_g	710185.0	N/m^2	supply gage pressure
R	287.0	m^2/sec^2-K	universal gas constant
γ	1.40	(dimensionless)	specific heat ratio
c_d	0.60	(dimensionless)	discharge coefficient
P_a	101000.0	N/m^2	atmospheric pressure
T	293.0	K	cylinder temperature
k_c	162000.0	N/m	simple cylinder spring
b_c	90000.0	N-sec/m	simple cylinder damper
g	9.80665	m/sec^2	gravitational acceleration

stop stiffness. Therefore, the constant chosen for k_h, given in the table, represents only the stiffness of the stop.

The elbow stiffness, k_e, was found by measuring force and deflection at the top of the upper arm with the lower arm fixed. The relation was observed to be linear within the accuracy of the measurements made, and the calculated value for k_e appears in the table.

The viscous damping constants, b_1, b_2, and b_h, for the three joints were estimated by matching the peak amplitudes predicted by the simulation output at the resonant frequencies with those observed in the experimental data at the same frequencies.

The coulomb friction observed in the pantograph was very low so the values c_1, c_2, and c_h were set to small values in the absence of a suitable model for the stiction which may have a greater effect.

The dimensions x_f, y_f, l_e, and θ_e^o which affect the elbow linkage kinematics were measured on the pantograph. The dimensions l_b and α, describing the short arm through which input torque is applied, were also measured in the laboratory and confirmed by the assembly drawings.

The piston area A_p and orifice area A_o were measured by removing the necessary parts from the cylinder. The cylinder initial volume V^o was calculated from the known cylinder dimensions. The supply gage pressure, P_g, was found from the regulator setpoint.

The values for the gas properties R and γ were found in tables. The discharge coefficient c_d describes a sharp orifice. The ambient pressure and temperature were used for P_a and T. For the simple cylinder model, the stiffness k_c describes the compression of the gas that would be trapped in the

cylinder if the orifice were blocked. A value for k_c was chosen by linearizing the compression of the ideal gas about the static pressure operating point. The value for the cylinder damping, b_c, was chosen by matching the linear cylinder pressure output to the experimental pressure data.

The usual value for the gravitational acceleration, g, was used.

Chapter 4
Experimental Model

An experiment was performed in the laboratory to verify that the nonlinear model is an accurate representation of a real pantograph. A Brecknell-Willis pantograph was instrumented, and its dynamic response to a range of displacement input recorded for analysis. This chapter discusses the dynamic testing conducted at the U.S. Department of Transportation's Transportation System Center (TSC) in Cambridge, Massachusetts.

4.1 Laboratory Setup

A Brecknell-Willis "high-speed" pantograph was obtained from Amtrak and set up in the TSC laboratory. The pantograph was fixed to a steel base plate, and a structure of steel beams erected to support a hydraulic input ram and instrumentation. A supply of compressed gas (nitrogen) was provided to operate the pneumatic system which raises the pantograph. Figure 4-1 depicts this laboratory setup.

The servo-controlled hydraulic ram simulated a sinusoidal catenary over a range of frequency. The ram, mounted above the pantograph, excited the system with a displacement input at the contacting carbons. A function generator provided the time-varying input signal to the servo controller. An LVDT measured the ram's position output for feedback and for reference.

In some tests, the ram was rigidly attached to the center of the carbons.

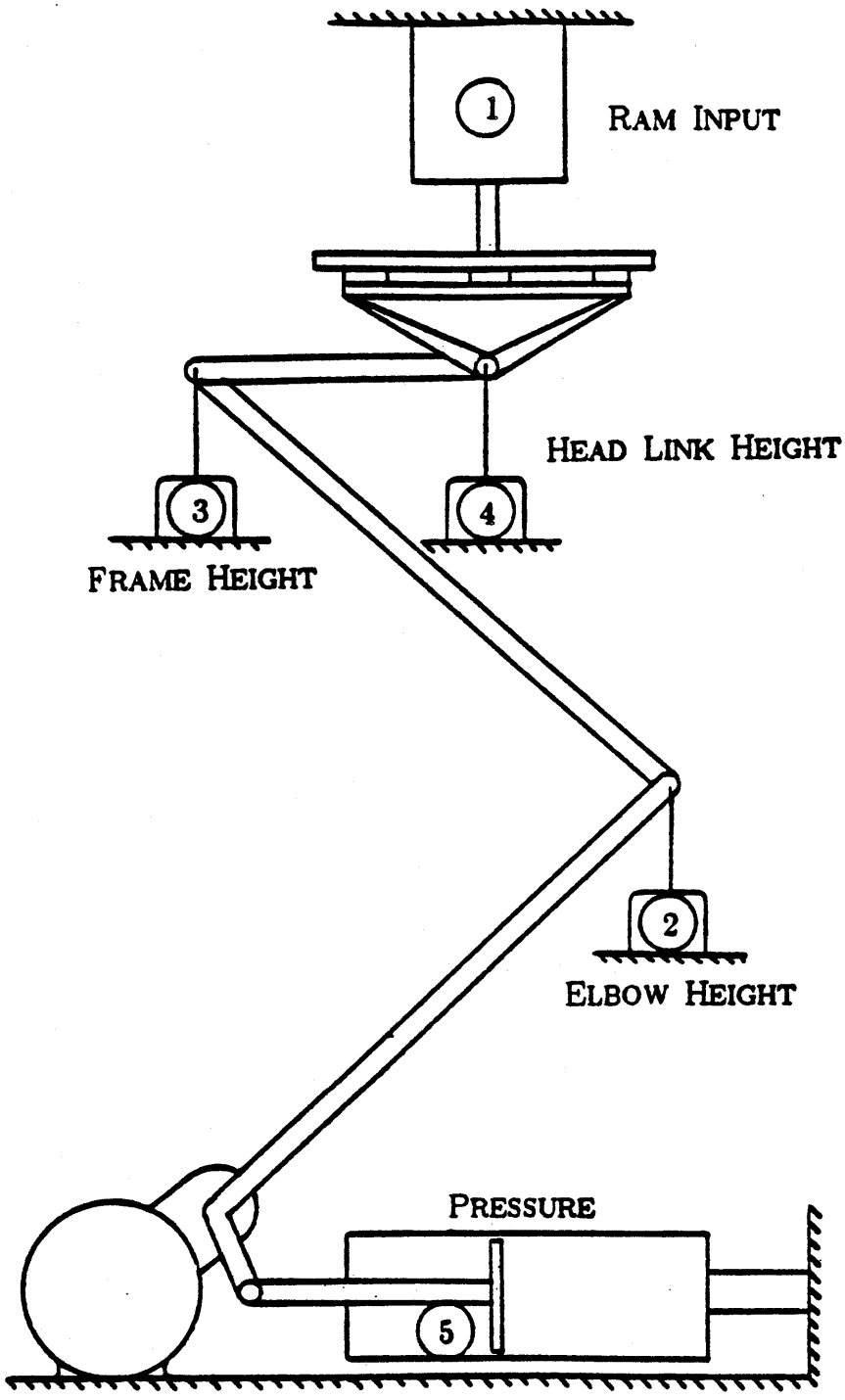

Figure 4-1: Experimental Pantograph Setup

This configuration corresponds to the simulated test case in which the catenary spring, k_s, can both push down and pull up on the head. Further tests were run in which the ram was not attached, and could only push down, which is case is more representative of the pantograph operating under a catenary.

Three position displacement transducers, by Celesco Transducers Products, measured the response of the three rotational state variables. These transducers, called stringpots, simply consist of precision conductive-plastic, rotary potentiometers that have cable wrapped around their input shafts with light return springs.

One stringpot, attached at the pantograph "elbow", measured the lower link position. The second stringpot, attached to a point at the top of the pantograph frame, recorded the overall motion. The remaining one measured the height of the end of the head link. The difference between the first two stringpot signals gave the upper frame link motion, while the difference between the second and third signals gave the head link motion. The potentiometers allowed the use of a simple voltage divider circuit to output a voltage proportional to linear displacement. The input voltage to each transducer was "tuned" to attain zero output at the static operating point.

A differential pressure transducer, by Validyne Engineering Corporation, measured the pneumatic cylinder pressure. One side of the diaphragm was maintained at the supply pressure, while the other side contained the cylinder pressure. In this configuration, the transducer output represents the pressure drop across the small orifice at the cylinder input. The transducer was of the variable-reluctance type, so it required an AC carrier signal and a demodulator to produce the desired DC output. A Tektronix differential amplifier was used to subtract the DC offset from the pressure signal.

A Racal FM data recorder was used to store the transducer outputs on magnetic tape for later analysis. Five channels of data were recorded:

1. ram LVDT output
2. elbow stringpot output
3. top-of-frame stringpot output
4. head stringpot output
5. pressure transducer output

The first signal records the time-varying input height, while the remaining four channels represent the response of the pantograph's four degrees of freedom, θ_1, θ_2, θ_h, and P.

4.2 Experimental Procedure

A summary of the experimental procedure follows.

After the pantograph and instrumentation were set up as described, pressure was applied to the pneumatic cylinder. To avoid the transient associated with filling the system to operating pressure, supply pressure was temporarily routed to both sides of the differential pressure transducer. This prevented damage to the diaphragm before the operating point was reached.

Next, the hydraulic pump and cooling system were started. With a low-frequency, zero-amplitude input signal, the servo controller was turned on.

The input voltage was applied to the stringpots, and the carrier signal to the pressure transducer. All five circuits, including the ram setpoint, were then tuned to achieve zero output at the static operating point. To maximize

the dynamic range of data stored on the tape recorder.

Then, with the desired frequency and amplitude set, the five channels of data were recorded onto the tape.

Data were taken at 0.5 Hz intervals from 1.0 to 15.0 Hz. Data were obtained for the cases with the head both rigidly attached to, and detached from the ram. Many input amplitudes were applied, and frequency was swept both up and down to observe various nonlinear effects.

The five (analog) channels of experimental data were digitized wtih an analog-to-digital (A/D) converter. The data were then processed digitally to obtain the desired output states.

4.3 Data Processing

The analog data were transported on magnetic tape to the Machine Dynamics Laboratory at M.I.T. The five channels were played back simultaneously with the Racal tape recorder into a Datel A/D converter on the Digital PDP 11/44 minicomputer in the laboratory. Each channel was sampled every 2 ms (500 Hz) for two seconds. The digital data were ouput to files for processing.

The raw data files were transferred on disk to M.I.T.'s Joint Computer Facility, where the processing was to be completed. The data arrays were scaled, first by the recording levels to obtain the recorder input voltage amplitudes, and then by the instrumentation sensitivities to find the actual pressure and displacement information. Next, the elbow column was subtracted from the top-of-frame column to obtain the displacements of the

upper link with respect to the lower link. The top-of-frame column was then subtracted from the head column to yield the head displacements with respect to the top of the frame. Finally, the five columns of data were slightly offset for plotting.

Of the 20 seconds of data recorded at each frequency of excitation, only 1.6 seconds were digitized, and only one second of data actually plotted.

Chapter 5
Results

A comparison is made of the two pantograph representations discussed in the previous chapters. The simulation output is compared with the processed experimental data to verify that the analytical model can be used to accurately predict the actual pantograph dynamics.

5.1 Simulation Output

The general pantograph model developed in Chapter Three was augmented with the linear cylinder and elbow models in order to describe the Brecknell-Willis pantograph tested.

The input height, y_w, was a sinusoidal displacement of peak-to-peak amplitude 3.7 mm added to the static operating height of 1.58 m. Input frequency ranged from 1.0 to 30.0 Hz.

In these simulations, the top spring, k_s, was able to apply forces both up and down to the head, modelling the case in which the ram was attached rigidly to the contacting carbons.

For the modelled system, which acts somewhat like a three-mass, four-spring system, we expect to observe three second-order resonances, and one first-order lag. In fact, we do see just that. The system resonances are at roughly 4.25 Hz, 8.75 Hz, and 19.5 Hz. The first-order cylinder state, P, always follows the lower frame link state θ_1, as expected. The time constant

describing the cylinder response is $\tau = \frac{b_c}{k_c}$.

The time histories output from the simulation each show four curves, which are labelled as follows:

- IN --- input displacement height, y_w
- HD --- head relative displacement, $l_h \sin\theta_h$
- F2 --- upper frame link relative displacement, $l_2 \sin\theta_2$
- F1 --- lower frame link displacement, $l_1 \sin\theta_1$

Figures 5-1 through 5-6 plot simulation output for six representative frequencies. The 2.0 Hz response, Figure 5-1, typifies the low-frequency vibrations. The two frame states are in phase with the input, and each frame link accounts for roughly half of the gross motion. There is very little rotation of the head link.

As the frequency is increased toward the first system resonance, however, the frame motions increase dramatically. Figure 5-2 shows the 3.5 Hz response. With more force now across the head, the head deflections also increase, but are out of phase with the input and frame motions.

The 4.5 Hz response shown in Figure 5-3 is very near the first system resonance. The output states have reached peak amplitudes, and they have shifted in phase. The frame states are about 90 degrees out of phase, while the head lags behind the input by nearly 270 degrees.

Well above the first resonance, Figure 5-4 shows the 6.5 Hz response, typical of the vibrations at frequencies between the first two resonances. The frame states have settled down considerably. The head, which is now in phase

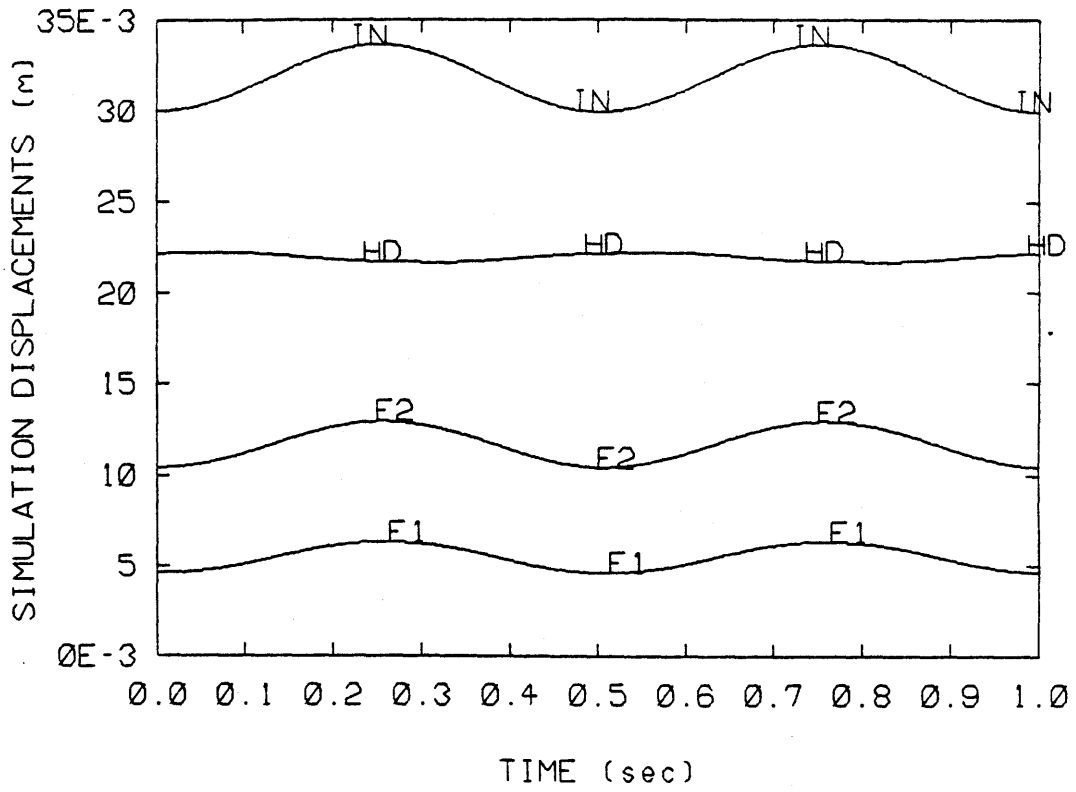

Figure 5-1: 2.0 Hz Simulation Time Response

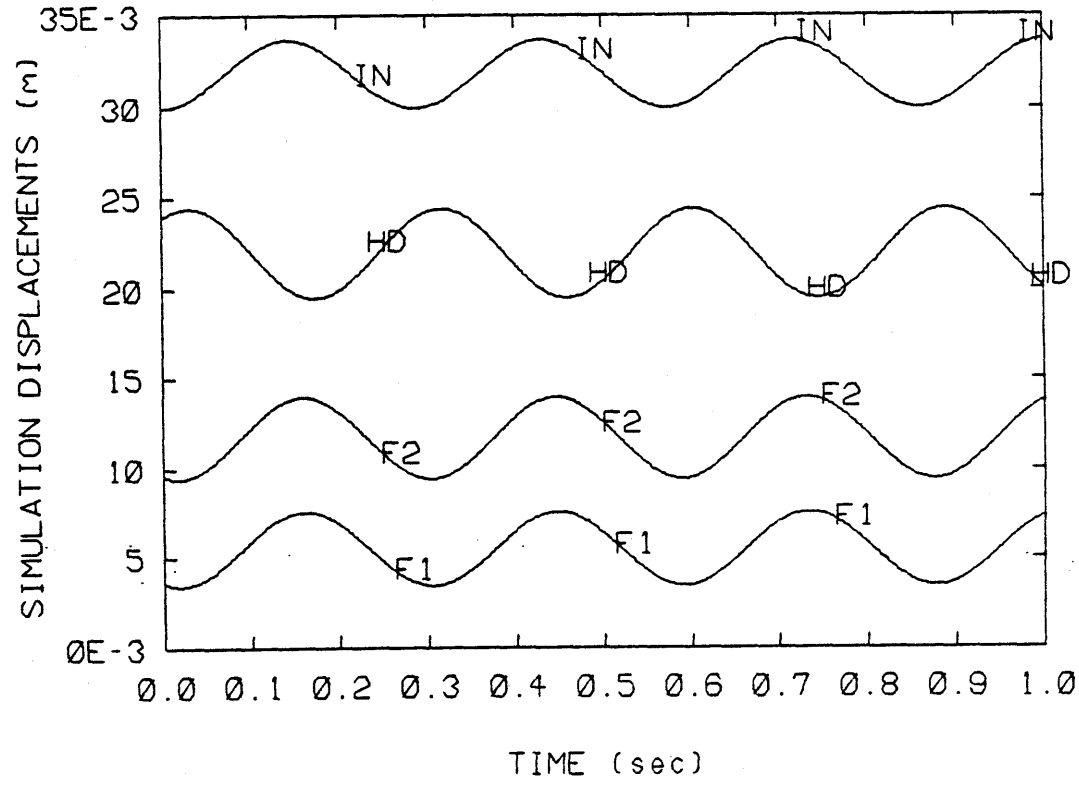

Figure 5-2: 3.5 Hz Simulation Time Response

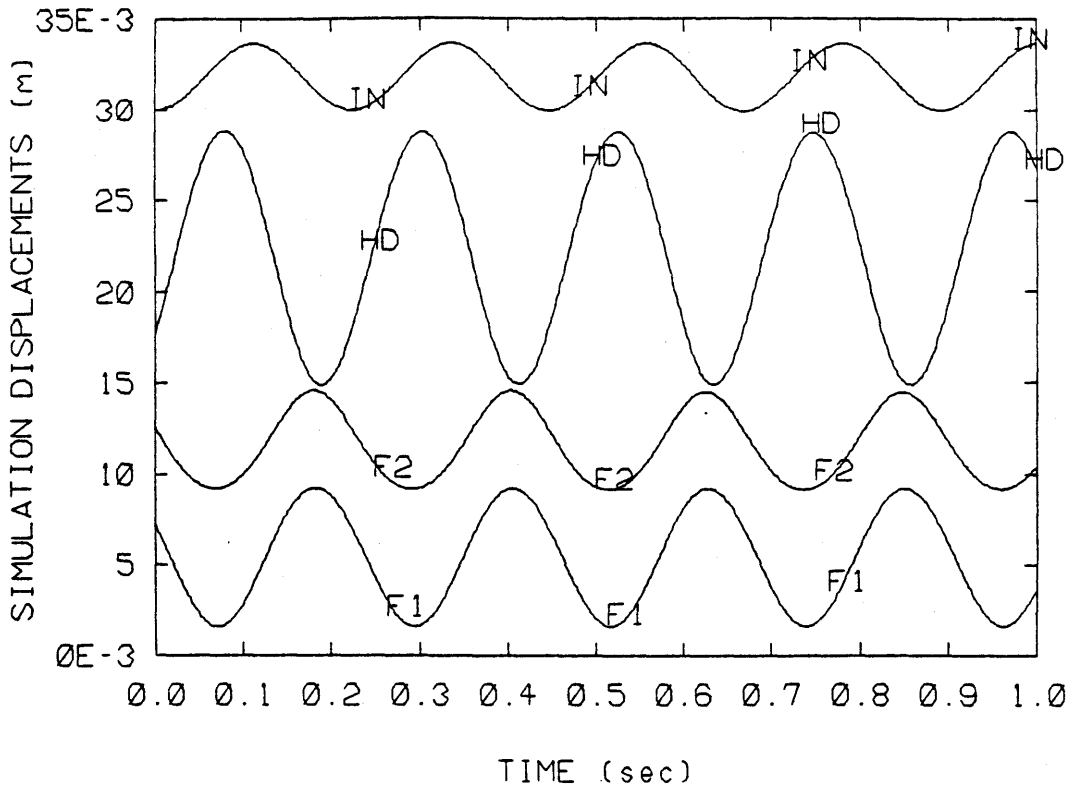

Figure 5-3: 4.5 Hz Simulation Time Response

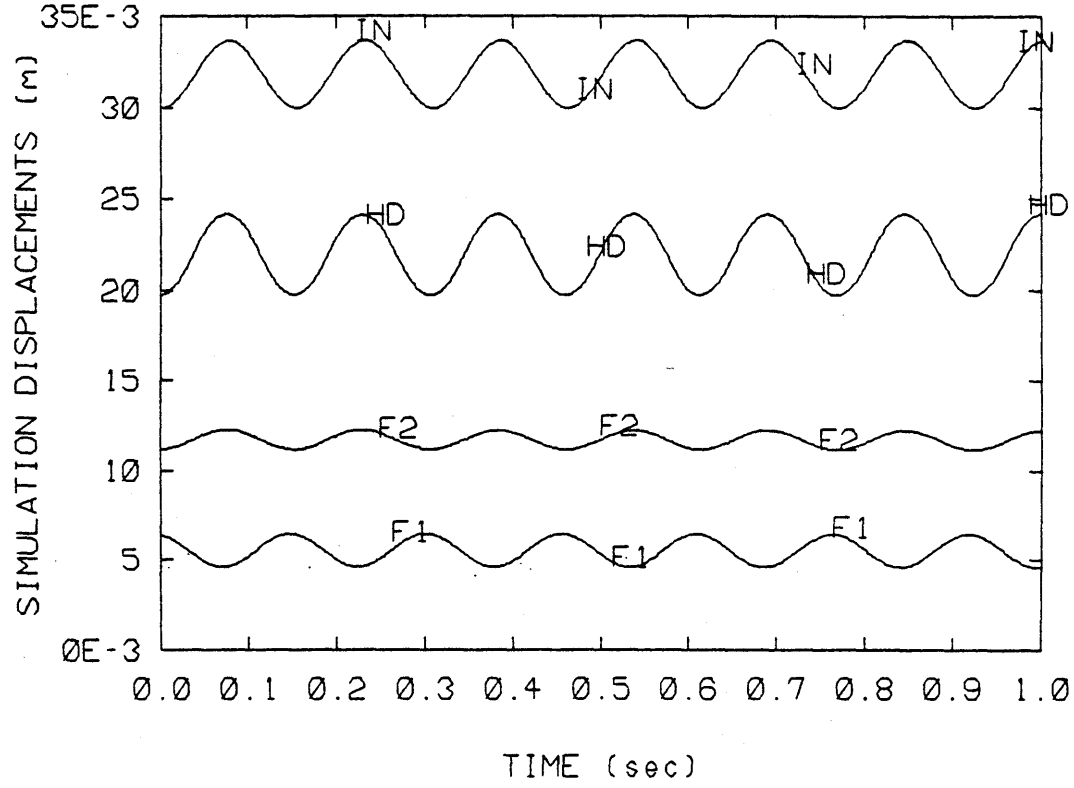

Figure 5-4: 6.5 Hz Simulation Time Response

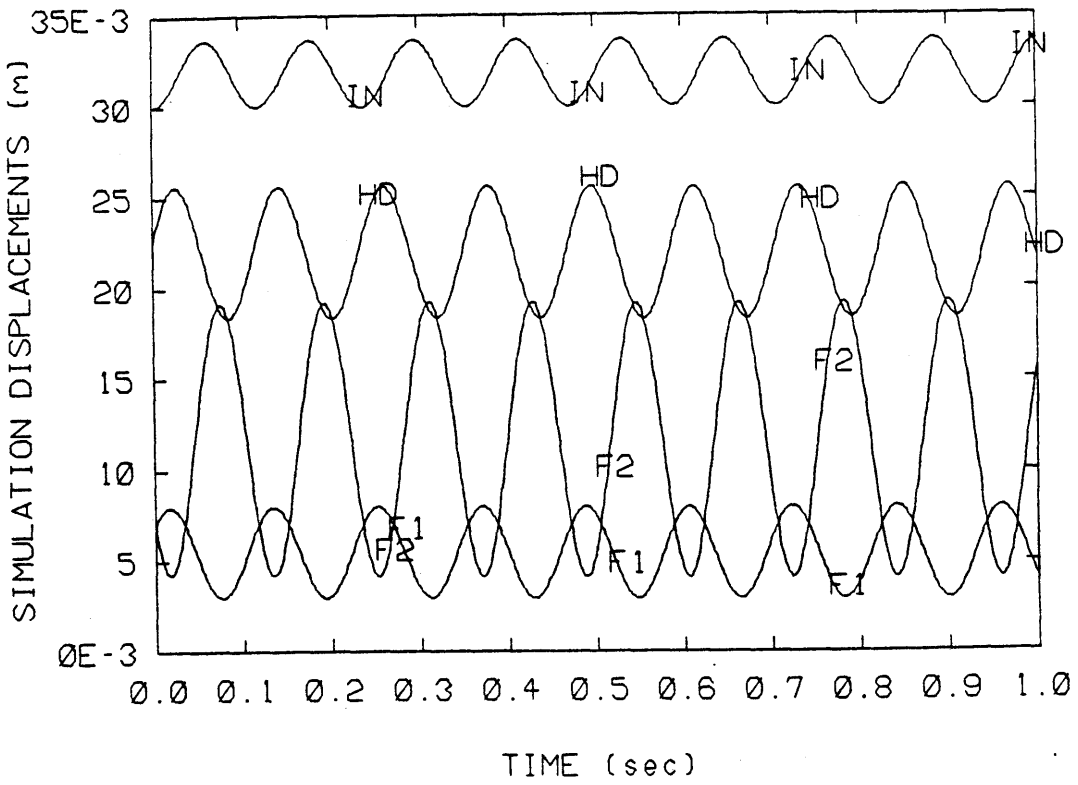

Figure 5-5: 8.5 Hz Simulation Time Response

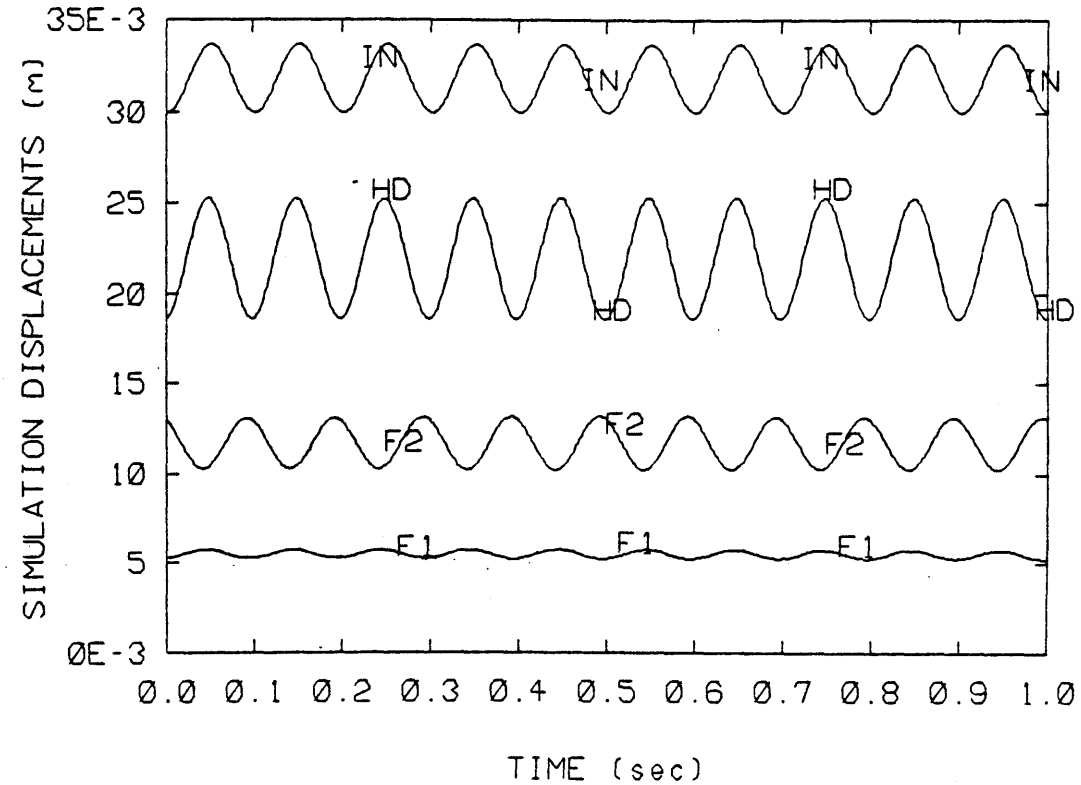

Figure 5-6: 10.0 Hz Simulation Time Response

with the input displacement, dominates the response. The two frame states have split in phase. The upper frame link is again in phase with the input, while the lower link is now almost 180 degrees out of phase.

The 8.5 Hz response, Figure 5-5, is very near the second system resonance. The states have again shifted by 90 degrees and reached peak amplitudes.

Figure 5-6 shows the 10.0 Hz response which typifies the system response to input frequencies above the second resonance. The head rotation is again in phase with the input displacement. However, with its amplitude greater than that of the input, the head motion causes the frame to be out of phase (the opposite of the situation just below the first resonance).

Since only a few frequencies are plotted here for brevity, while many more cases were simulated, a graphic aid is used to visualize the system's total frequency response. If the system were linear, we could make a Bode plot to show the frequency response. For the nonlinear pantograph model simulated, at low amplitudes of excitation and small levels of coulomb friction, the vibrations about an operating point would be nearly linear. For comparison with the experimental results only, we can make a frequency response plot in the style of a Bode plot. The plot is valid only for the specific operating height and input amplitude for which it is drawn. Figure 5-7 shows this frequency repsonse plot for the simulation output discussed.

The actual simulated response, of course, is nonlinear. Each point on the amplitude plot was then determined by considering only the component at the forcing frequency, and evaluating the output amplitude and phase with respect to the input.

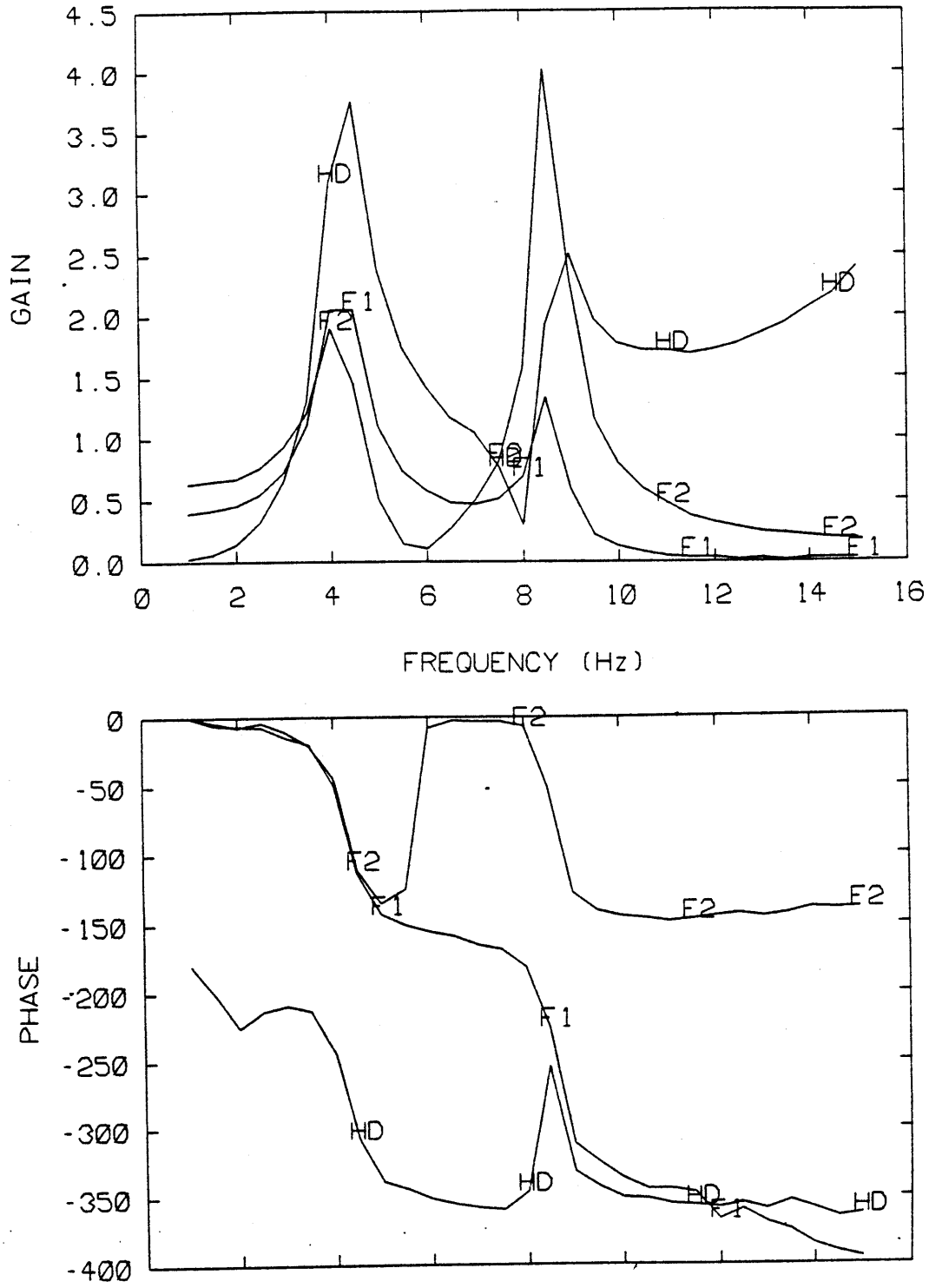

Figure 5-7: Frequency Response of the Nonlinear Model

5.2 Experimental Data

The test pantograph was set up in the laboratory, instrumented, and tested as described in Chapter Four. The experimental data were processed and are presented here for comparison with the simulation output.

The static operating height of 1.58 m and the sinusoidal input displacement amplitude of 3.7 mm peak-to-peak compare to those used in the model implementation. However, unlike the digital simulation's constant-amplitude input displacement, the servo-controlled hydraulic ram cannot maintain the desired response for all situations. The experimental input displacement is therefore neither purely sinusoidal, nor of constant amplitude.

Again, while many tests were conducted, only a few sample results are reproduced here for comparison. Input frequencies ranged from 1.0 Hz to 15.0 Hz. In the cases presented below, the contacting shoe was rigidly attached to the ram.

Insight gained from the modelling has led us to expect to observe three system resonances and to find the pressure state responding only to the lower frame link motions. The first two resonances appear near 4.0 Hz and 8.25 Hz. The third resonance falls at a frequency above the test range. The cylinder pressure response was as expected and, for clarity, is not included in the plots below.

The time histories obtained from the experimental data are each presented as four curves. The states represent the same ones output from the simulation, and are labelled as follows:

- IN --- input displacement

- HD --- head displacement with respect to top of frame
- F2 --- upper frame link displacement with respect to elbow
- F1 --- lower frame link displacement

Figures 5-8 through 5-13 contain experimental data plotted for six representative frequencies.

Figure 5-8 shows the 2.0 Hz response. The two frame states dominate the response, each taking roughly half the input amplitude. The amount of head rotation is small at low frequency and out of phase, as expected.

The system response at 3.5 Hz, shown in Figure 5-9, shows the frame states increasing in amplitude as the first resonance is approached. The greater frame response induces large head motions 180 degrees out of phase with the input.

Figure 5-10 shows the 4.0 Hz response, very near the first system resonance. All three of the states now lag almost 90 degrees from their low-frequency phase relations. The large-amplitude motions display one of the nonlinear effects not shown in the smaller vibrations. The model does not predict this harmonic response at double the input frequency.

Past the first resonance, the 6.0 Hz response plotted in Figure 5-11 shows the head with an amplitude greater than that of the input displacement, and in phase. The two frame states have split phase as predicted, with the upper link back in phase with the input, and the lower link 180 degrees out of phase.

Figure 5-12 shows the system response at 8.0 Hz, very near the second resonance. All the states are approaching peak amplitudes and are again

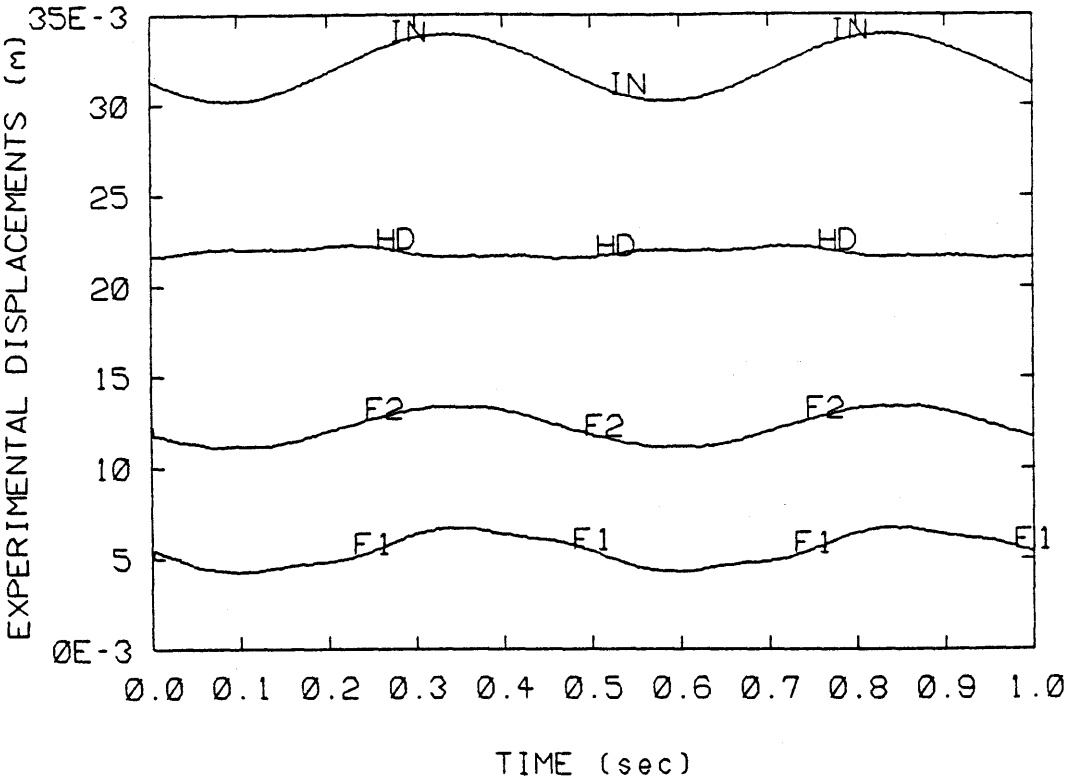

Figure 5-8: 2.0 Hz Experimental Data

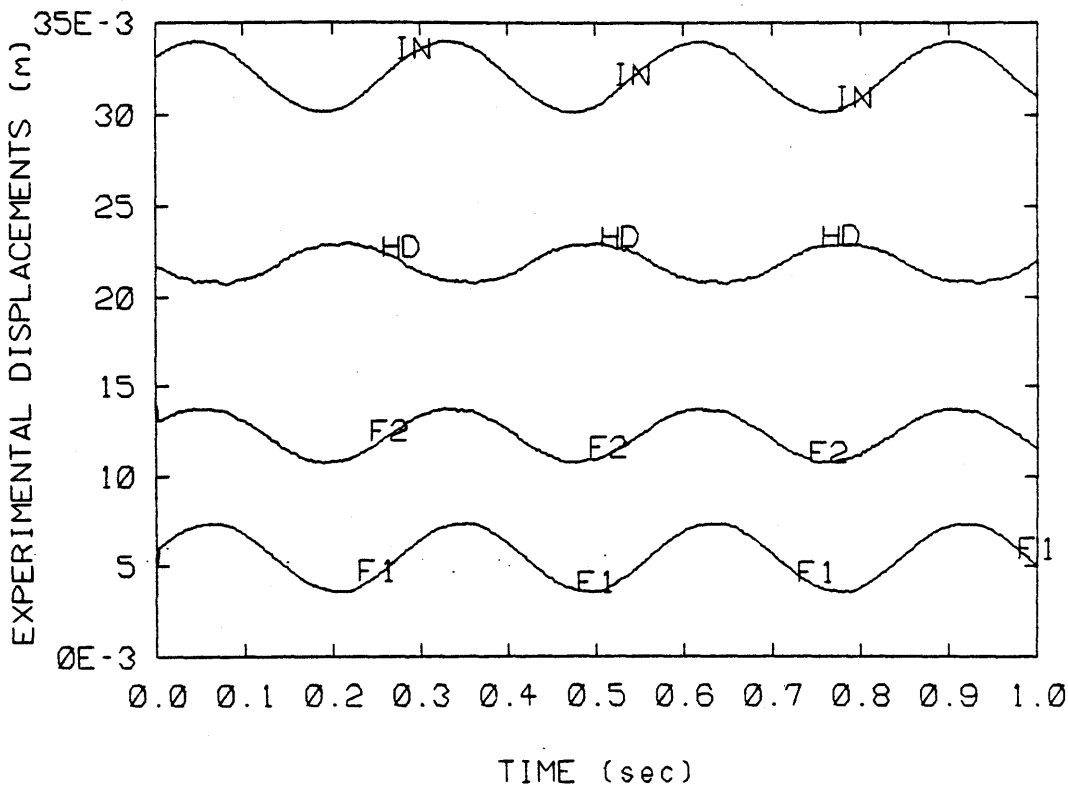

Figure 5-9: 3.5 Hz Experimental Data

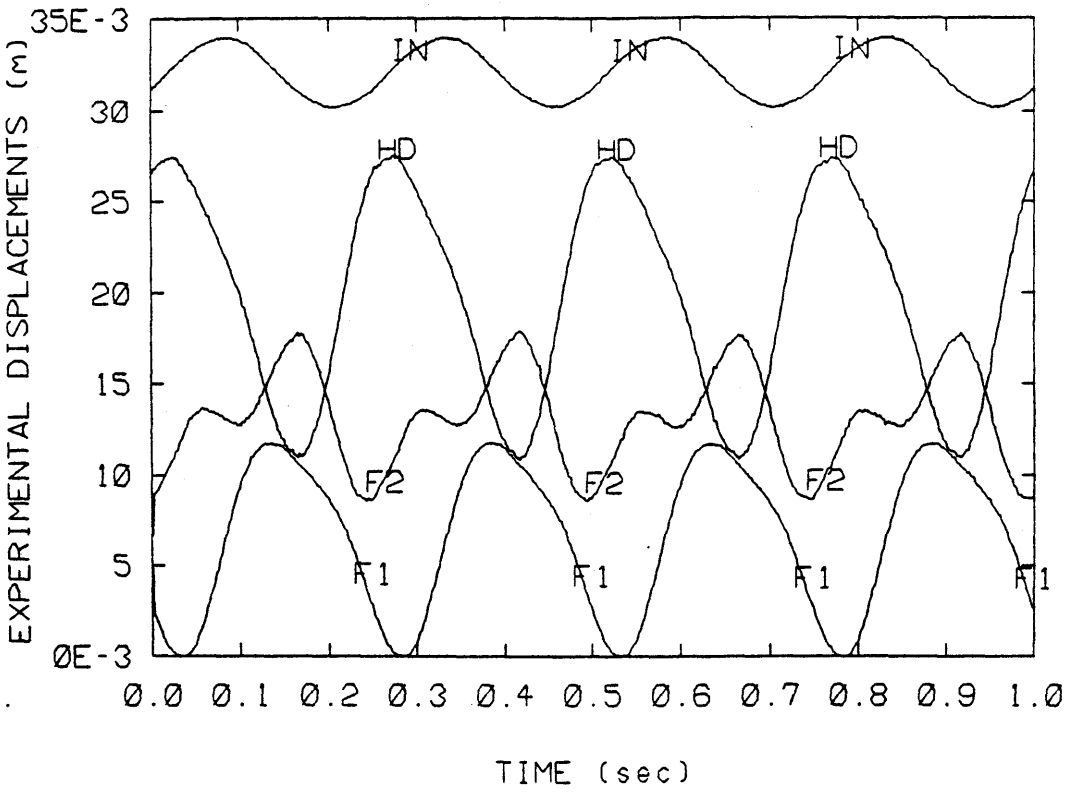

Figure 5-10: 4.0 Hz Experimental Data

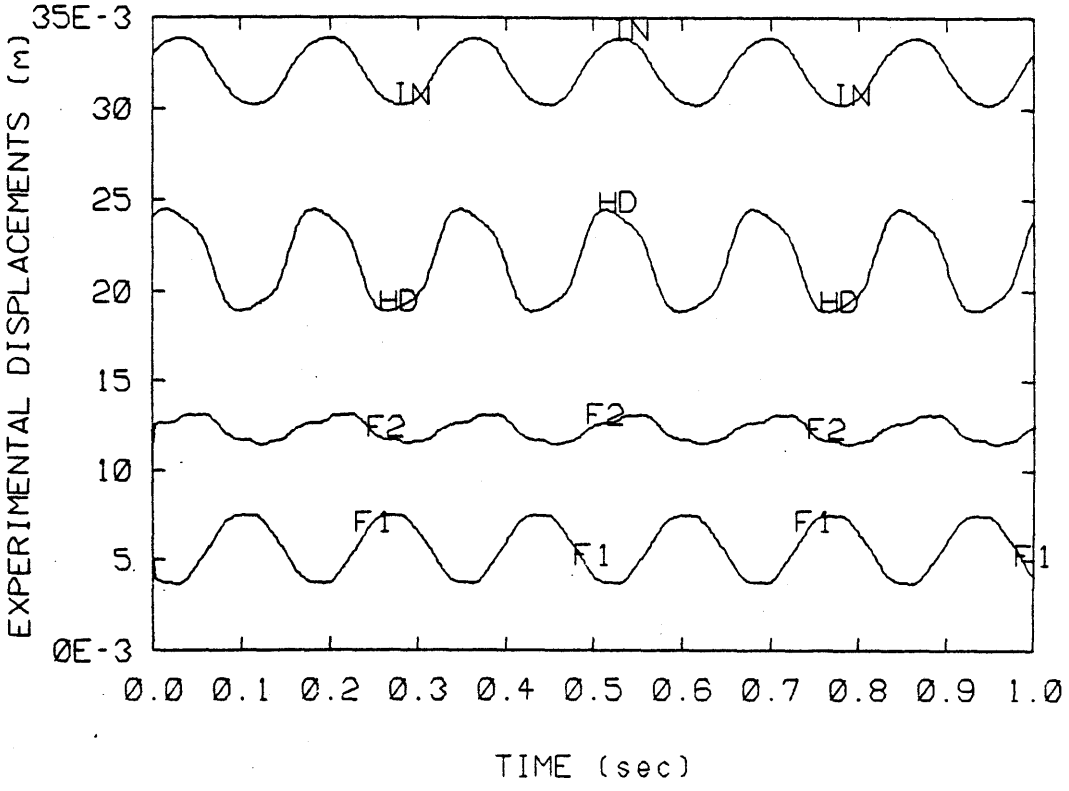

Figure 5-11: 6.0 Hz Experimental Data

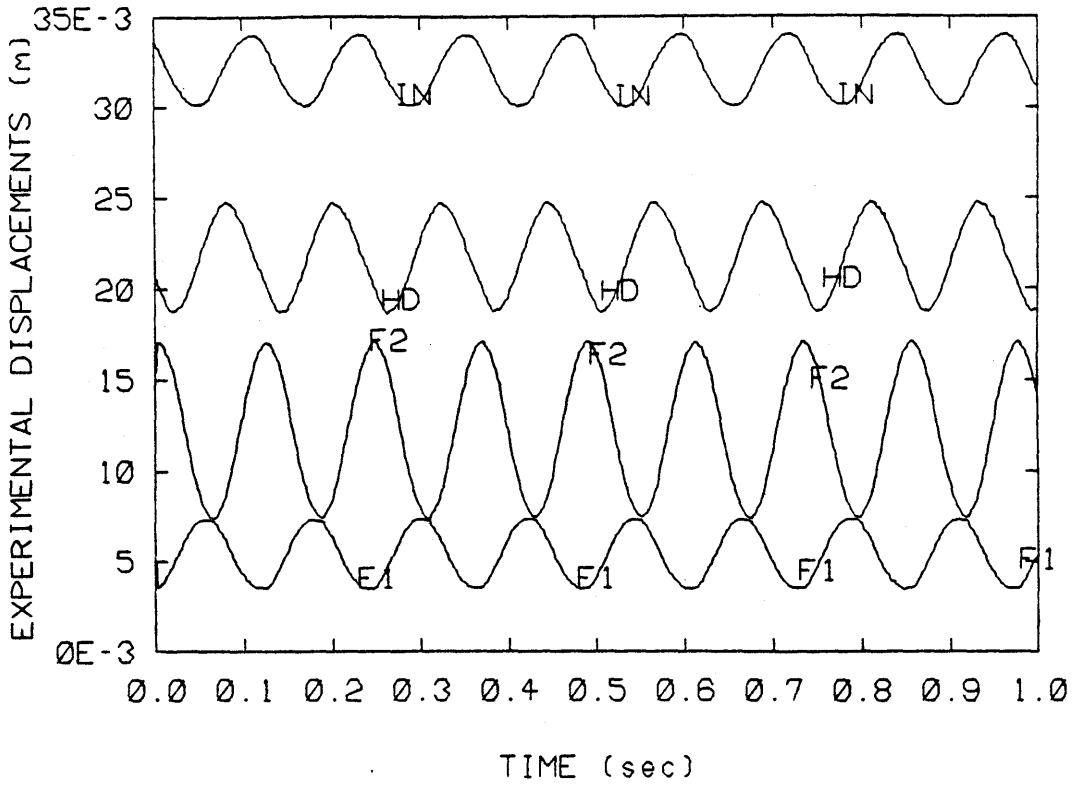

Figure 5-12: 8.0 Hz Experimental Data

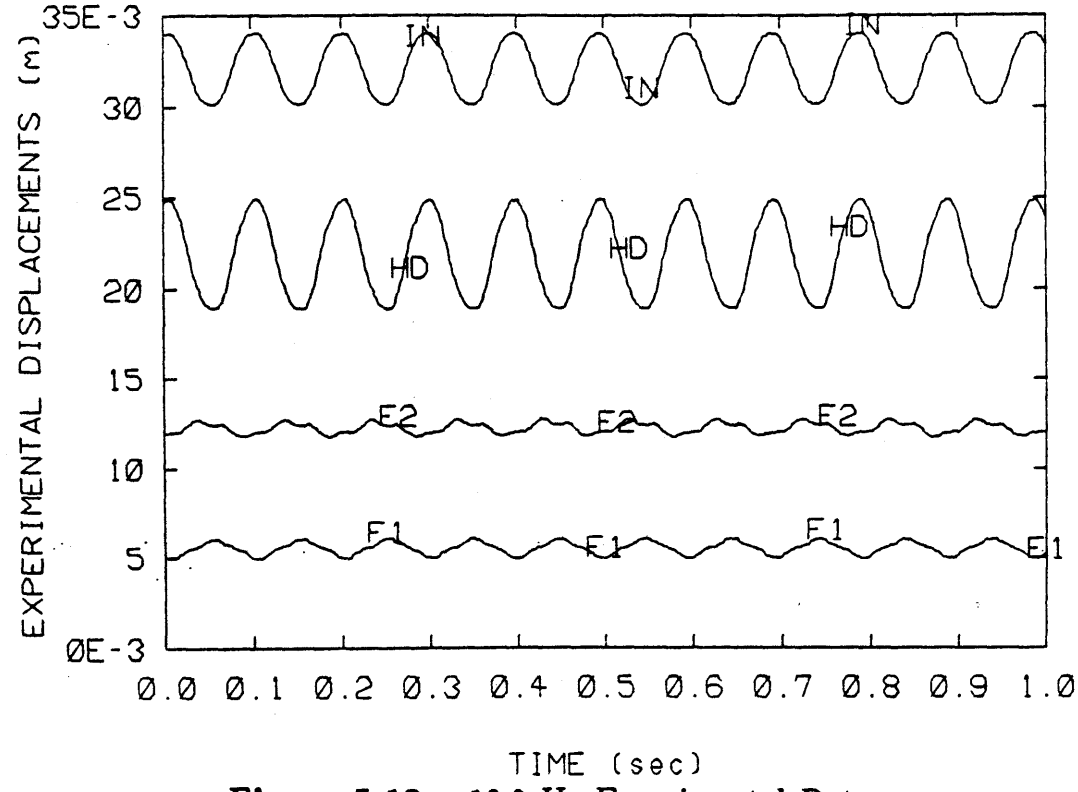

Figure 5-13: 10.0 Hz Experimental Data

shifting in phase.

Above the second resonance, Figure 5-13 shows the 10.0 Hz response. The head is now in phase with the input and dominates the response. The two frame states are out of phase with the input and have a lower amplitude, as expected.

As with the simulation output, we will again attempt to summarize the frequency response graphically as if the system were linear. Taking only the peak amplitude of the response at each input frequency, we can make a frequency response plot which approximates the system performance only at the specific operating point and input amplitude tested. Figure 5-14 shows this plot for the experimental data discussed.

5.3 Model Verification

The frequency response plots for the simulated and actual pantographs are sketched in Figures 5-7 and 5-14, respectively. The two systems share many common traits yet there are some distinct differences. For comparison, these two plots which represent the system responses under similar conditions are discussed.

At low frequency, the model correctly predicts both the amplitude and phase of the head state. The model shows the lower frame link taking less than half the input amplitude, and the upper link having correspondingly more. This is the effect of the kinematic elbow relation, which must be slightly off. The experimental data plotted suggest that $\frac{\delta\theta_e}{\delta\theta_1}$ is near 1.0, while the model shows that $\frac{\delta\theta_e}{\delta\theta_1}$ is much higher, perhaps 1.4, since the upper link moves more than the lower link in the quasi-static case.

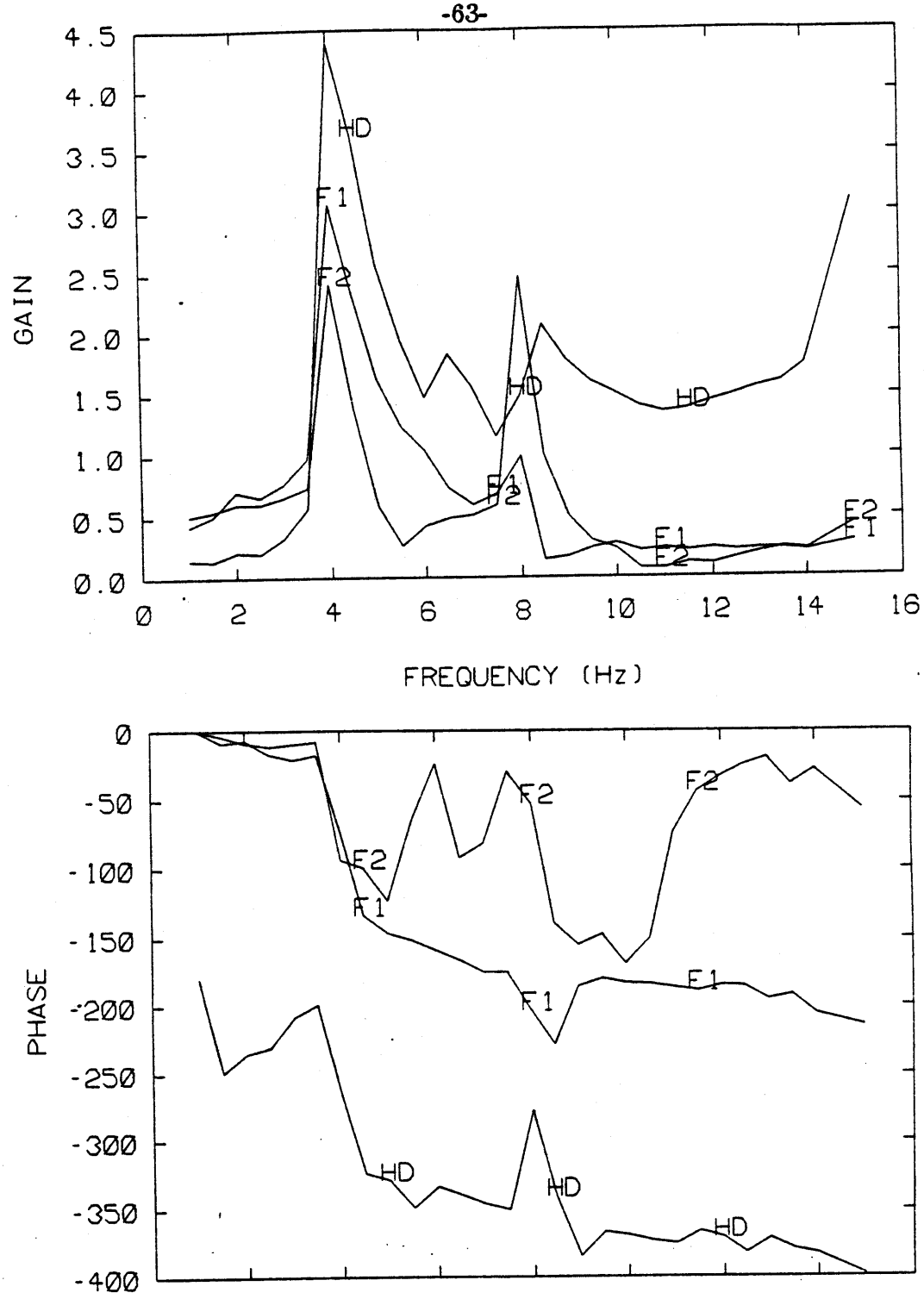

Figure 5-14: Frequency Response of the Experimental Pantograph

The frequency of and peak amplitudes at the first resonance are well shown by the model (considering the resolution along the frequency axis). The phase shifts and splitting of the frame states are also remarkably well predicted.

At 6.5 Hz, the experimental data displays a definite jump in head amplitude and a temporary shift in the upper link phase. The model shows no such changes. These phenomena suggest another resonance, perhaps structural, which is not modelled in the simulation.

The frequency of the second resonance is slightly off; however, the relative amplitudes of the states are fairly well predicted by the model. There is some discrepancy in the phase shifts at this resonance.

Above 10 Hz, the model correctly predicts the amplitudes of the states, including the rise before the next resonance. Frame phase relationships, on the other hand, are wrong above the second resonance; however, with the very low amplitudes of frame motion at these frequencies, the consequence of this divergence may be small. Failure of the model to accurately represent this phase information may be attributable to inaccuracies caused by the limitations of the simple, linear cylinder model.

In conclusion, the nonlinear model describing the Brecknell-Willis pantograph accurately predicts the fundamental response amplitudes through 15 Hz, and phases through the second resonance, near 9 Hz.

The model developed can now be used to study many new configurations of high-speed pantographs. The model can be used in conjunction with catenary simulations developed in order to study the pantograph/catenary interaction.

Chapter 6
Conclusions and Recommendations

6.1 Dynamic Model Development

A nonlinear model was developed to predict the response of a pantograph. The model was used to describe a Brecknell-Willis Pantograph. The actual device was instrumented and tested in the laboratory. The experimental data were compared with the simulation output in order to confirm the validity of the model.

The results, presented in the previous chapter, show that the simulation is able to produce the system response for input frequencies through the second modelled resonance. The pantograph's resonant frequencies near 4.25 and 8.25 Hz were closely predicted by the model. The proper amplitudes and phase shifts are shown by the simulation results both before and after the first resonance. However, at 6.5 Hz there is an unmodelled resonance, one which shows up in the experimental data and not in the simulation output causing a discrepancy only in the response amplitudes very near 6.5 Hz. At the higher frequencies, above 9 Hz, the model predicts the amplitudes of motions correctly, but not the phase.

In general, the model developed has proven to be quite robust. The nonlinear model well predicted the dynamics of the physical system, including some features of the response which could not have been matched by a linear model.

The model assumes all of the links to be rigid; however, in the physical system these members can flex, so there are many more resonances than actually modelled. If the system response must be predicted with more accuracy or at higher frequencies, adequate models of structural effects would have to be included.

Elbow modelling has a great effect on system performance. One cannot assume the knuckle of an asymmetrical pantograph to be infinitely stiff. O'Connor [12] showed that frame motions are a very important factor in dynamic performance, and the results presented here show that the two frame links do not always move together, so an accurate elbow model is essential.

The cylinder model may also significantly influence overall performance. Its effect should be studied in more depth. In addition, the kinematics of the upper arm could be included in the model to provide a more accurate "datum angle" to reference the head link's torsional spring.

6.2 Recommendations for Use

The successful nonlinear pantograph model development warrants its implementation into a complete pantograph/catenary dynamic simulation. The pantograph model is ready for use with any catenary model that can interface through a contact spring.

The catenary model developed as part of this research [1], [12], and [20], accepts contact force from the pantograph in each timestep and returns the new wire height to the pantograph [21], while the two systems are integrated simultaneously.

Finally, both the complete pantograph/catenary simulation and the nonlinear pantograph model itself will be very useful in parameter studies aimed at determining the parameters which seriously affect overall system performance.

References

[1] Armbruster, K.
Modelling and Dynamics of Pantograph-Catenary Systems for High Speed Trains.
Master's thesis, Massachusetts Institute of Technology, 1983.

[2] Belyaev, I. A., Vologine, V. A., and Freifeld, A. V.
Improvement of Pantograph and Catenary and Method of Calculating Their Mutual Interactions at High Speeds.
Rail International , June, 1977.

[3] Blackburn, John F., Reethof, Gerhard, and Shearer, J. Lowen.
Fluid Power Control.
MIT Press, Cambridge, Massachusetts, 1960.

[4] Boissonnade, Pierre.
Catenary Design for High Speeds.
Rail International , March, 1975.

[5] Boissonnade, Pierre, and Dupont, Robert.
SNCF Tests Collection Systems for High Speeds.
International Railway Journal , October, 1975.

[6] Boissonnade, Pierre, and Dupont, Robert.
Current Collection With Two-Stage Pantographs on the New Paris-Lyon Line.
Railway Gazette International , October, 1977.

[7] Communications of the O. R. E.
Behavior of Pantographs and Overhead Equipment at Speeds Above 160 km/hr.
Rail International , January, 1972.

[8] Coxen, D. J., Gostling, R. J., and Whitehead, K. M.
Evolution of a Simple High-Performance Pantograph.
Railway Gazette , January, 1980.

[9] Crandall, Stephen H., et al.,
Dynamics of Mechanical and Electromechanical Systems.
McGraw Hill, New York, New York, 1968.

[10] Faux, I. D. and Pratt, M. J.
Computational Geometry for Design and Manufacture.
Ellis Horwood, Chichester, West Sussex, England, 1981.

[11] Gostling, R. J. and Hobbs, A. E. W.
The Interactions of Pantographs and Overhead Equipment: Practical Applications of a New Theoretical Method.
Technical Report, Institute of Mechanical Engineers, Derby Branch, February, 1981.

[12] O'Connor, D.
Modelling and Simulation of Pantograph-Catenary Systems.
Master's thesis, Massachusetts Institute of Technology, 1984.

[13] Peters, John.
Dead Line Testing of the Faiveley Single and Dual Stage Pantographs on the RTT Catenary Systems.
Technical Report FRA/TCC-81/01, U.S. Department of Transportation, 1981.

[14] Sikorsky Aircraft.
Design and Development of a Servo-Operated Pantograph for High Speed Trains.
Final Report Contract Number 7-35415, U.S. Department of Transportation, July, 1970.

[15] Simmons, George F.
Differential Equations with Applications and Historical Notes.
McGraw-Hill, New York, New York, 1972.

[16] Strang, Gilbert.
Linear Algebra and Its Applications.
Academic Press, New York, New York, 1980.

[17] Vesely, G. C.
Modelling and Experimentation of Pantograph Dynamics.
Master's thesis, Massachusetts Institute of Technology, 1983.

[18] Vinayagalingam, T.
Computer Evaluation of Controlled Pantographs for Current Collection From Simple Catenary Overhead Equipment at High Speed.
Journal of Dynamic Systems, Measurement, and Control , December, 1983.

[19] Wann, L. M.
Improvement of a Pantograph for High Speed Train.
Master's thesis, Massachusetts Institute of Technology, 1980.

[20] Wormley, D. N., Seering, W. P., Armbruster, K., and Vesely, G. C.
Dynamic Performance Characteristics of New Configuration Pantograph-Catenary Systems.
First Annual Report, Grant Number DT-RS-56-81-C-00020, U.S. Department of Transportation, December, 1982.

[21] Wormley, D. N., Seering, W. P., Eppinger, S. D., and O'Connor, D. N.
Dynamic Performance Characteristics of New Configuration Pantograph-Catenary Systems.
Final Report, Grant Number DT-RS-56-81-C-00020, U.S. Department of Transportation, May, 1984.

Appendix A
Derivation of Governing Equations

The equations of motion for the nonlinear pantograph model shown in Figure A-1 are derived using Lagrange's energy-based method. The three generalized coordinates are θ_1, θ_2, and θ_h. Each of the three links has a mass m_i, an inertia I_i, a length l_i, and a distance to its center of mass d_i. The height, y_w, is the displacement input from the catenary, and F_c is the external force applied by the suspension (pneumatic cylinder). The force F_c is applied through a moment arm of length l_b at a fixed angle α with respect to the lower link. Viscous damping and coulomb friction act at each joint. These dissipative terms have the parameters b_1, b_2, b_h, c_1, c_2, and c_h.

The kinetic co-energy is first written as a sum of simple energy terms which include the motion of the three links.

$$T^* = \tfrac{1}{2}(I_1+m_1d_1^2)\dot{\theta}_1^2 + \tfrac{1}{2}I_2\dot{\theta}_2^2 + \tfrac{1}{2}m_2(\dot{x}_2^2+\dot{y}_2^2) + \tfrac{1}{2}I_h\dot{\theta}_h^2 + \tfrac{1}{2}m_h(\dot{x}_h^2+\dot{y}_h^2) \qquad \text{(A.1)}$$

where the x- and y-coordinates are used to describe the positions of the masses with respect to the axes drawn.

$$x_2 = l_1\cos\theta_1 - d_2\cos\theta_2 \qquad \text{(A.2)}$$

$$y_2 = l_1\sin\theta_1 + d_2\sin\theta_2 \qquad \text{(A.3)}$$

$$x_h = l_1\cos\theta_1 - l_2\cos\theta_2 + d_h\cos\theta_h \qquad \text{(A.4)}$$

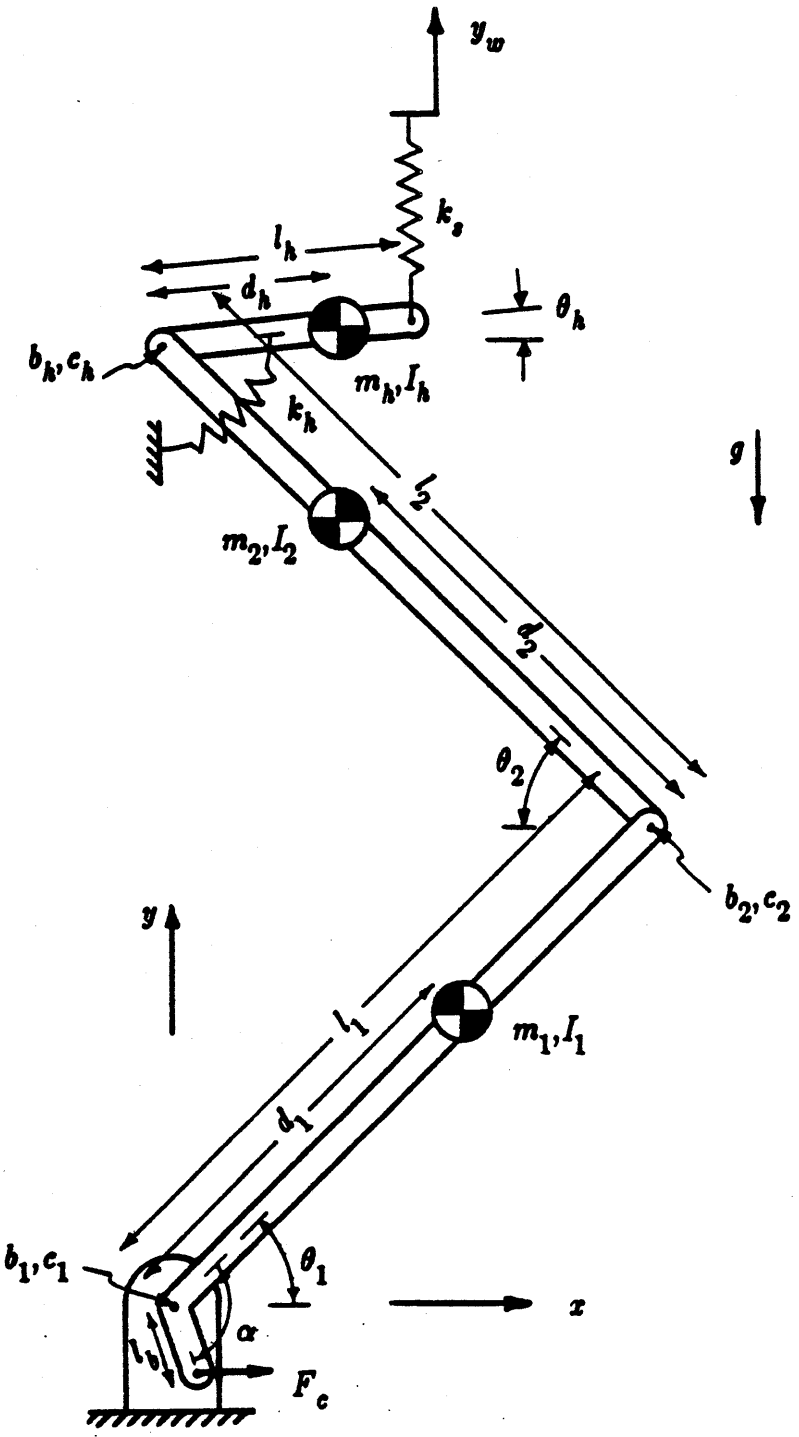

Figure A-1: General Pantograph Model

$$y_h = l_1\sin\theta_1 + l_2\sin\theta_2 + d_h\sin\theta_h \tag{A.5}$$

and differentiating to obtain the velocities,

$$\dot{x}_2 = - l_1\dot{\theta}_1\sin\theta_1 + d_2\dot{\theta}_2\sin\theta_2 \tag{A.6}$$

$$\dot{y}_2 = l_1\dot{\theta}_1\cos\theta_1 + d_2\dot{\theta}_2\cos\theta_2 \tag{A.7}$$

$$\dot{x}_h = - l_1\dot{\theta}_1\sin\theta_1 + l_2\dot{\theta}_2\sin\theta_2 - d_h\dot{\theta}_h\sin\theta_h \tag{A.8}$$

$$\dot{y}_h = l_1\dot{\theta}_1\cos\theta_1 + l_2\dot{\theta}_2\cos\theta_2 + d_h\dot{\theta}_h\cos\theta_h \tag{A.9}$$

The potential energy is written by summing the energy stored in the springs and the potential from gravity.

$$V = \tfrac{1}{2}k_h\theta_h^2 + \tfrac{1}{2}k_s(y_w - y_d)^2 + m_1gy_1 + m_2gy_2 + m_hgy_h \tag{A.10}$$

where

$$y_d = l_1\sin\theta_1 + l_2\sin\theta_2 + l_h\sin\theta_h \tag{A.11}$$

$$y_1 = d_1\sin\theta_1 \tag{A.12}$$

$$y_2 = l_1\sin\theta_1 + d_2\sin\theta_2 \tag{A.13}$$

$$y_h = l_1\sin\theta_1 + l_2\sin\theta_2 + d_h\sin\theta_h \tag{A.14}$$

The non-conservative work is written by summing all the work done onto the system by the external force, viscous damping, and coulomb friction.

$$\sum F_{nc}\cdot\delta r_{nc} = F_c l_b\sin(\alpha - \theta_1)\delta\theta_1$$

$$
\begin{aligned}
&- b_1\dot{\theta}_1\delta\theta_1 - b_2(\dot{\theta}_1+\dot{\theta}_2)(\delta\theta_1+\delta\theta_2) - b_h(\dot{\theta}_2+\dot{\theta}_h)(\delta\theta_2+\delta\theta_h) \\
&- c_1\mathrm{sgn}(\dot{\theta}_1)\delta\theta_1 - c_2\mathrm{sgn}(\dot{\theta}_1+\dot{\theta}_2)(\delta\theta_1+\delta\theta_2) \\
&- c_h\mathrm{sgn}(\dot{\theta}_2+\dot{\theta}_h)(\delta\theta_2+\delta\theta_h) \qquad \text{(A.15)}
\end{aligned}
$$

Now substituting to solve for the energies in terms of the generalized coordinates only,

$$
\begin{aligned}
T^* = {} & \tfrac{1}{2}[I_1+m_1d_1^2]\dot{\theta}_1^2 + \tfrac{1}{2}I_2\dot{\theta}_2^2 + \tfrac{1}{2}I_h\dot{\theta}_h^2 \\
& + \tfrac{1}{2}m_2[l_1^2\sin^2\theta_1\dot{\theta}_1^2 + d_2^2\sin^2\theta_2\dot{\theta}_2^2 - 2l_1d_2\sin\theta_1\sin\theta_2\dot{\theta}_1\dot{\theta}_2 \\
& \qquad + l_1^2\cos^2\theta_1\dot{\theta}_1^2 + d_2^2\cos^2\theta_2\dot{\theta}_2^2 + 2l_1d_2\cos\theta_1\cos\theta_2\dot{\theta}_1\dot{\theta}_2] \\
& + \tfrac{1}{2}m_h[l_1^2\sin^2\theta_1\dot{\theta}_1^2 + l_2^2\sin^2\theta_2\dot{\theta}_2^2 + d_h^2\sin^2\theta_h\dot{\theta}_h^2 \\
& \qquad - 2l_1l_2\sin\theta_1\sin\theta_2\dot{\theta}_1\dot{\theta}_2 + 2l_1d_h\sin\theta_1\sin\theta_h\dot{\theta}_1\dot{\theta}_h \\
& \qquad - 2l_2d_h\sin\theta_2\sin\theta_h\dot{\theta}_2\dot{\theta}_h \\
& \qquad + l_1^2\cos^2\theta_1\dot{\theta}_1^2 + l_2^2\cos^2\theta_2\dot{\theta}_2^2 + d_h^2\cos^2\theta_h\dot{\theta}_h^2 \\
& \qquad + 2l_1l_2\cos\theta_1\cos\theta_2\dot{\theta}_1\dot{\theta}_2 + 2l_1d_h\cos\theta_1\cos\theta_h\dot{\theta}_1\dot{\theta}_h \\
& \qquad + 2l_2d_h\cos\theta_2\cos\theta_h\dot{\theta}_2\dot{\theta}_h] \qquad \text{(A.16)}
\end{aligned}
$$

and

$$
\begin{aligned}
V = {} & \tfrac{1}{2}k_h\theta_h^2 \\
& + \tfrac{1}{2}k_s[y_w^2 + l_1^2\sin\theta_1^2 + l_1^2\sin\theta_2^2 + l_h^2\sin\theta_h^2 \\
& \qquad - 2y_wl_1\sin\theta_1 - 2y_wl_2\sin\theta_2 - 2y_wl_h\sin\theta_h \\
& \qquad + 2l_1l_2\sin\theta_1\sin\theta_2 + 2l_1l_h\sin\theta_1\sin\theta_h + 2l_2l_h\sin\theta_2\sin\theta_h] \\
& + m_1gd_1\sin\theta_1 + m_2g(l_1\sin\theta_1 + d_2\sin\theta_2) \\
& + m_hg(l_1\sin\theta_1 + l_2\sin\theta_2 + d_h\sin\theta_h). \qquad \text{(A.17)}
\end{aligned}
$$

Combining terms,

$$
\begin{aligned}
T^* = {} & \dot{\theta}_1^2[\tfrac{1}{2}(I_1+m_1 d_1^2) + \tfrac{1}{2}m_2 l_1^2 + \tfrac{1}{2}m_h l_1^2] \\
& + \dot{\theta}_2^2[\tfrac{1}{2}I_2 + \tfrac{1}{2}m_2 d_2^2 + \tfrac{1}{2}m_h l_2^2] \\
& + \dot{\theta}_h^2[\tfrac{1}{2}I_h + \tfrac{1}{2}m_h d_h^2] \\
& + \dot{\theta}_1\dot{\theta}_2[(m_2 l_1 d_2+m_h l_1 l_2)(\cos\theta_1\cos\theta_2-\sin\theta_1\sin\theta_2)] \\
& + \dot{\theta}_1\dot{\theta}_h[m_h l_1 d_h(\sin\theta_1\sin\theta_h+\cos\theta_1\cos\theta_h)] \\
& + \dot{\theta}_2\dot{\theta}_h[m_h l_2 d_h(\cos\theta_2\cos\theta_h-\sin\theta_2\sin\theta_h)]
\end{aligned}
\tag{A.18}
$$

and

$$
\begin{aligned}
V = {} & \theta_h^2(\tfrac{1}{2}k_h) \\
& + \sin^2\theta_1(\tfrac{1}{2}k_s l_1^2) \\
& + \sin^2\theta_2(\tfrac{1}{2}k_s l_2^2) \\
& + \sin^2\theta_h(\tfrac{1}{2}k_s l_h^2) \\
& + \sin\theta_1\sin\theta_2(k_s l_1 l_2) \\
& + \sin\theta_1\sin\theta_h(k_s l_1 l_h) \\
& + \sin\theta_2\sin\theta_h(k_s l_2 l_h) \\
& + \sin\theta_1(-k_s y_w l_1 + m_1 g d_1 + m_2 g l_1 + m_h g l_1) \\
& + \sin\theta_2(-k_s y_w l_2 + m_2 g d_2 + m_h g l_2) \\
& + \sin\theta_h(-k_s y_w l_h + m_h g d_h) \\
& + \tfrac{1}{2}k_s y_w^2
\end{aligned}
\tag{A.19}
$$

The external torques are found from the non-conservative work by using the relation

$$\sum F_{nc}\cdot\delta r_{nc} = \sum \Xi_i \delta\theta_i \qquad \text{for } i = 1,\ 2,\ \text{and } h. \tag{A.20}$$

The external torques are found to be

$$\Xi_1 = F_c l_b \sin(\alpha-\theta_1) - b_1\dot{\theta}_1 - b_2(\dot{\theta}_1+\dot{\theta}_2) - c_1\mathrm{sgn}(\dot{\theta}_1) - c_2\mathrm{sgn}(\dot{\theta}_1+\dot{\theta}_2) \tag{A.21}$$

$$\Xi_2 = -b_2(\dot{\theta}_1+\dot{\theta}_2) - b_h(\dot{\theta}_2+\dot{\theta}_h) - c_2\mathrm{sgn}(\dot{\theta}_1+\dot{\theta}_2) - c_h\mathrm{sgn}(\dot{\theta}_2+\dot{\theta}_h) \tag{A.22}$$

$$\Xi_h = -b_h(\dot{\theta}_2+\dot{\theta}_h) - c_h\mathrm{sgn}(\dot{\theta}_2+\dot{\theta}_h). \tag{A.23}$$

Now we form the Lagrangian,

$$L = T^* - V \tag{A.24}$$

and use Lagrange's equation to write the governing equations:

$$\frac{\mathrm{d}}{\mathrm{dt}}\left(\frac{\partial L}{\partial \dot{\theta}_i}\right) - \left(\frac{\partial L}{\partial \theta_i}\right) = \Xi_i \qquad \text{for } i = 1,\ 2,\ \text{and } h. \tag{A.25}$$

For $i = 1$, we find the first governing equation by differentiating.

$$\frac{\mathrm{d}}{\mathrm{dt}}\left(\frac{\partial L}{\partial \dot{\theta}_1}\right) - \left(\frac{\partial L}{\partial \theta_1}\right) = \Xi_1 \tag{A.26}$$

$$\begin{aligned}
&\ddot{\theta}_1[I_1 + m_1 d_1^2 + m_2 l_1^2 + m_h l_1^2] \\
&+ \ddot{\theta}_2[(m_2 l_1 d_2 + m_h l_1 l_2)(\cos\theta_1\cos\theta_2 - \sin\theta_1\sin\theta_2)] \\
&+ \ddot{\theta}_h[m_h l_1 d_h(\sin\theta_1\sin\theta_h + \cos\theta_1\cos\theta_h)] \\
&- \dot{\theta}_2(\dot{\theta}_1+\dot{\theta}_2)(\sin\theta_1\cos\theta_2 + \cos\theta_1\sin\theta_2)(m_2 l_1 d_2 + m_h l_1 l_2)
\end{aligned}$$

$$
\begin{aligned}
&- \dot{\theta}_h(\dot{\theta}_1-\dot{\theta}_h)(\sin\theta_1\cos\theta_h-\cos\theta_1\sin\theta_h)m_h l_1 d_h \\
&= - \dot{\theta}_1\dot{\theta}_2(m_2 l_1 d_2+m_h l_1 l_2)(\cos\theta_1\sin\theta_2+\sin\theta_1\cos\theta_2) \\
&+ \dot{\theta}_1\dot{\theta}_h(m_h l_1 d_h)(\cos\theta_1\sin\theta_h-\sin\theta_1\cos\theta_h) \\
&- [\cos\theta_1(-k_s y_w l_1+m_1 g d_1+m_2 g l_1+m_h g l_1) \\
&+ \sin\theta_1\cos\theta_1(k_s l_1^2) + \cos\theta_1\sin\theta_2(k_s l_1 l_2) + \cos\theta_1\sin\theta_h(k_s l_1 l_h)] \\
&+ F_c l_b\sin(\alpha-\theta_1) - b_1\dot{\theta}_1 - b_2(\dot{\theta}_1+\dot{\theta}_2) \\
&- c_1\mathrm{sgn}(\dot{\theta}_1) - c_2\mathrm{sgn}(\dot{\theta}_1+\dot{\theta}_2)
\end{aligned}
\tag{A.27}
$$

Combining terms,

$$
\begin{aligned}
&\ddot{\theta}_1[I_1 + m_1 d_1^2 + m_2 l_1^2 + m_h l_1^2] \\
&+ \ddot{\theta}_2[(m_2 l_1 d_2+m_h l_1 l_2)\cos(\theta_1+\theta_2)] \\
&+ \ddot{\theta}_h[m_h l_1 d_h\cos(\theta_1-\theta_h)] \\
&= \dot{\theta}_2^2(m_2 l_1 d_2+m_h l_1 l_2)\sin(\theta_1+\theta_2) \\
&+ \dot{\theta}_h^2(m_h l_1 d_h)\sin(\theta_h-\theta_1) \\
&+ \cos\theta_1(k_s y_w l_1-m_1 g d_1-m_2 g l_1-m_h g l_1) \\
&- \sin\theta_1\cos\theta_1(k_s l_1^2) - \cos\theta_1\sin\theta_2(k_s l_1 l_2) - \cos\theta_1\sin\theta_h(k_s l_1 l_h) \\
&+ F_c l_b\sin(\alpha-\theta_1) - b_1\dot{\theta}_1 - b_2(\dot{\theta}_1+\dot{\theta}_2) \\
&- c_1\mathrm{sgn}(\dot{\theta}_1) - c_2\mathrm{sgn}(\dot{\theta}_1+\dot{\theta}_2).
\end{aligned}
\tag{A.28}
$$

For $i = 2$, we find the second governing equation by differentiating.

$$
\frac{\mathrm{d}}{\mathrm{dt}}\left(\frac{\partial \mathcal{L}}{\partial \dot{\theta}_2}\right) - \left(\frac{\partial \mathcal{L}}{\partial \theta_2}\right) = \Xi_2 \tag{A.29}
$$

$$
\ddot{\theta}_2[I_2+m_2 d_2^2+m_h l_2^2]
$$

$$
\begin{aligned}
&+ \ddot{\theta}_1[(m_2 l_1 d_2 + m_h l_1 l_2)(\cos\theta_1\cos\theta_2 - \sin\theta_1\sin\theta_2)] \\
&+ \ddot{\theta}_h[m_h l_2 d_h(\cos\theta_2\cos\theta_h - \sin\theta_2\sin\theta_h)] \\
&- \dot{\theta}_1(\dot{\theta}_1+\dot{\theta}_2)(m_2 l_1 d_2 + m_h l_1 l_2)(\sin\theta_1\cos\theta_2 + \cos\theta_1\sin\theta_2) \\
&- \dot{\theta}_h(\dot{\theta}_h+\dot{\theta}_2) m_h l_2 d_2(\cos\theta_2\sin\theta_h + \sin\theta_2\cos\theta_h) \\
&= - \dot{\theta}_1\dot{\theta}_2(m_2 l_1 d_2 + m_h l_1 l_2)(\sin\theta_1\cos\theta_2 + \cos\theta_1\sin\theta_2) \\
&- \dot{\theta}_2\dot{\theta}_h(m_h l_2 d_h)(\cos\theta_2\sin\theta_h + \sin\theta_2\cos\theta_h) \\
&- [\cos\theta_2(-k_s y_w l_2 + m_2 g d_2 + m_h g l_2) \\
&+ \sin\theta_2\cos\theta_2(k_s l_2^2) + \sin\theta_1\cos\theta_2(k_s l_1 l_2) + \cos\theta_2\sin\theta_h(k_s l_2 l_h)] \\
&- b_2(\dot{\theta}_1+\dot{\theta}_2) - b_h(\dot{\theta}_2+\dot{\theta}_h) - c_2\mathrm{sgn}(\dot{\theta}_1+\dot{\theta}_2) - c_h\mathrm{sgn}(\dot{\theta}_2+\dot{\theta}_h)
\end{aligned}
\tag{A.30}
$$

Combining terms,

$$
\begin{aligned}
&\ddot{\theta}_1[(m_2 l_1 d_2 + m_h l_1 l_2)\cos(\theta_1+\theta_2)] \\
&+ \ddot{\theta}_2[I_2 + m_2 d_2^2 + m_h l_2^2] \\
&+ \ddot{\theta}_h[m_h l_2 d_h \cos(\theta_2+\theta_h)] \\
&= \dot{\theta}_1^2(m_2 l_1 d_2 + m_h l_1 l_2)\sin(\theta_1+\theta_2) \\
&+ \dot{\theta}_h^2(m_h l_2 d_h)\sin(\theta_2+\theta_h) \\
&+ \cos\theta_2(k_s y_w l_2 - m_2 g d_2 - m_h g l_2) \\
&- \sin\theta_2\cos\theta_2(k_s l_2^2) - \sin\theta_1\cos\theta_2(k_s l_1 l_2) - \cos\theta_2\sin\theta_h(k_s l_2 l_h) \\
&- b_2(\dot{\theta}_1+\dot{\theta}_2) - b_h(\dot{\theta}_2+\dot{\theta}_h) - c_2\mathrm{sgn}(\dot{\theta}_1+\dot{\theta}_2) - c_h\mathrm{sgn}(\dot{\theta}_2+\dot{\theta}_h).
\end{aligned}
\tag{A.31}
$$

For $i = h$, we find the third governing equation by differentiating.

$$
\frac{\mathrm{d}}{\mathrm{dt}}\left(\frac{\partial \mathcal{L}}{\partial \dot{\theta}_h}\right) - \left(\frac{\partial \mathcal{L}}{\partial \theta_h}\right) = \Xi_h \tag{A.32}
$$

$$
\begin{aligned}
&\ddot{\theta}_h[I_h+m_h d_h^2] \\
&+ \ddot{\theta}_1[m_h l_1 d_h(\sin\theta_1\sin\theta_h+\cos\theta_1\cos\theta_h)] \\
&+ \ddot{\theta}_2[m_h l_2 d_h(\cos\theta_2\cos\theta_h-\sin\theta_2\sin\theta_h)] \\
&- \dot{\theta}_1(\dot{\theta}_1-\dot{\theta}_h)m_h l_1 d_h(\sin\theta_1\cos\theta_h-\cos\theta_1\sin\theta_h) \\
&- \dot{\theta}_2(\dot{\theta}_2+\dot{\theta}_h)m_h l_2 d_h(\sin\theta_2\cos\theta_h+\cos\theta_2\sin\theta_h) \\
&= \dot{\theta}_1\dot{\theta}_h(m_h l_1 d_h)(\sin\theta_1\cos\theta_h-\cos\theta_1\sin\theta_h) \\
&- \dot{\theta}_2\dot{\theta}_h(m_h l_2 d_h)(\sin\theta_2\cos\theta_h+\cos\theta_2\sin\theta_h) \\
&- [\theta_h k_h + \cos\theta_h(-k_s y_w l_h+m_h g d_h) \\
&+ \sin\theta_h\cos\theta_h(k_s l_h^2) + \sin\theta_1\cos\theta_h(k_s l_1 l_h) + \sin\theta_2\cos\theta_h(k_s l_2 l_h)] \\
&- b_h(\dot{\theta}_2+\dot{\theta}_h) - c_h\mathrm{sgn}(\dot{\theta}_2+\dot{\theta}_h)
\end{aligned}
\tag{A.33}
$$

Combining terms,

$$
\begin{aligned}
&\ddot{\theta}_1[m_h l_1 d_h\cos(\theta_1-\theta_h)] \\
&+ \ddot{\theta}_2[m_h l_2 d_h\cos(\theta_2+\theta_h)] \\
&+ \ddot{\theta}_h[I_h+m_h d_h^2] \\
&= \dot{\theta}_1^2(m_h l_1 d_h)\sin(\theta_1-\theta_h) \\
&+ \dot{\theta}_2^2(m_h l_2 d_h)\sin(\theta_2+\theta_h) \\
&+ \cos\theta_h(k_s y_w l_h - m_h g d_h) - \sin\theta_h\cos\theta_h(k_s l_h^2) \\
&- \sin\theta_1\cos\theta_h(k_s l_1 l_h) - \sin\theta_2\cos\theta_h(k_s l_2 l_h) \\
&- \theta_h k_h - b_h(\dot{\theta}_2+\dot{\theta}_h) - c_h\mathrm{sgn}(\dot{\theta}_2+\dot{\theta}_h).
\end{aligned}
\tag{A.34}
$$

Appendix B
Lower Arm Kinematics

The kinematic equations governing the lower arm of the Brecknell-Willis pantograph are derived from its linkage geometry. The elbow link angle, θ_e, and its time derivative, $\dot{\theta}_e$, are derived as functions of the lower arm position and velocity, θ_1 and $\dot{\theta}_1$.

The lower arm linkage is sketched in Figure B-1. The mechanism position is described by the angles θ_1, θ_e, and ϕ_1. The link geometry is fixed by the link length, l_1, the radius, l_e, the dimensions x_f and y_f, and the initial condition θ_e^o.

The equation of the line describing the link with angle ϕ_1 is

$$(\tan\phi_1)x - y - (y_f + x_f\tan\phi_1) = 0. \tag{B.1}$$

The distance from the pinion center to the line is then found from [10] and equated with l_e.

$$l_e^2 = \frac{[(\tan\phi_1 l_1\cos\theta_1 - l_1\sin\theta_1 - (y_f + x_f\tan\phi_1)]^2}{\tan^2\phi_1 + 1} \tag{B.2}$$

Combining terms, we have a quadratic equation in $\tan\phi_1$ which can be written as

$$A\tan^2\phi_1 + B\tan\phi_1 + C = 0,$$

where $A = (l_1\cos\theta_1 - x_f)^2 - l_e^2$

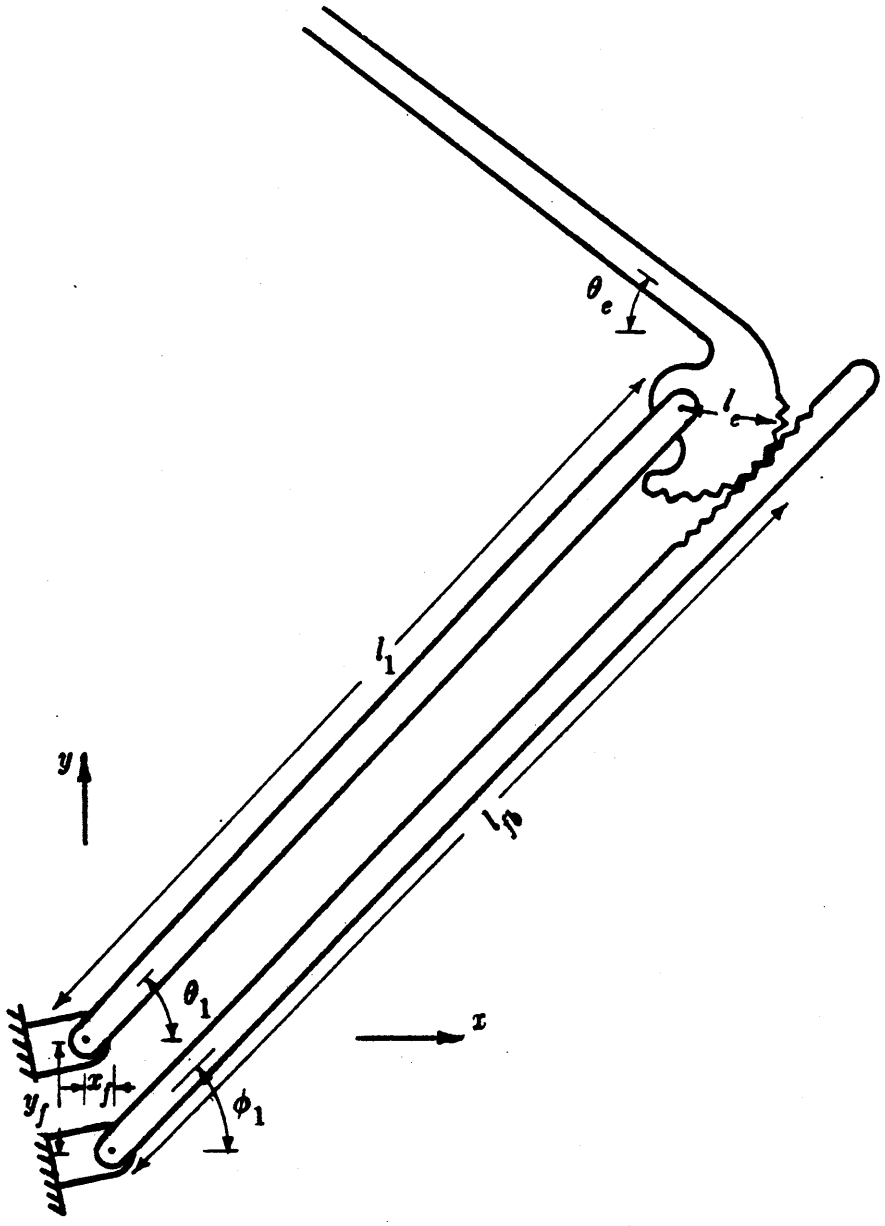

Figure B-1: Brecknell-Willis Lower Arm Linkage

$$B = -2(l_1\cos\theta_1 - x_f)(l_1\sin\theta_1 + y_f)$$

$$\text{and } C = (l_1\sin\theta_1 + y_f)^2 - l_e^2. \tag{B.3}$$

The solution to this equation is found from the quadratic formula where the negative root is taken.

$$\phi_1 = \arctan\left(\frac{-B - \sqrt{B^2 - 4AC}}{2A}\right) \tag{B.4}$$

Now the length of the "fourth bar" is written in terms of the angles θ_1 and ϕ_1.

$$l_{fb} = \sqrt{(l_1\cos\theta_1 + l_e\sin\phi_1 - x_f)^2 + (l_1\sin\theta_1 - l_e\cos\phi_1 + y_f)^2} \tag{B.5}$$

Finally, the rotation of the pinion is found to be

$$\theta_e = \theta_e^o - \frac{l_{fb}^o}{l_e} + \frac{l_{fb}}{l_e} - \theta_1 \tag{B.6}$$

where the initial conditions l_{fb}^o and θ_e^o are the values of l_{fb} and θ_e respectively when θ_1=0.

Appendix C
Simulation Program

The following is the FORTRAN code of the simulation subroutine EQSIM, used in conjunction with the software package DYSYS.

```
C
C   SIMULATION OF BRECKNELL-WILLIS PANTOGRAPH DYNAMICS
C
C   By Steven D. Eppinger          June 1983 through May 1984
C

      SUBROUTINE EQSIM

      COMMON T,DT,Y(30),FY(30),STIME,FTIME,NEWDT,NEWRUN,N
     &       IPR,ICD,ICN,TBREAK,PNEXT,TBACK,CONSTANT(30)

      REAL L1,L2,LH,M1,M2,MH,I1,I2,IH,KS,KH,NIA,LMARM,NA,
     &     IK1,JK1,KK1,LK1,LK2,LK3,LK4,LK5,LK6,LK7,LY3,
     &     I,J,K,L,KE,JAIB,KAIC,LAID,LE,LC1MXF,LS1PYF,KCYL
C
C   Equate state and auxilliary variables to array elements.
C
      EQUIVALENCE (Y(1),TH1)
      EQUIVALENCE (Y(2),TH1D)
      EQUIVALENCE (Y(3),TH2)
      EQUIVALENCE (Y(4),TH2D)
      EQUIVALENCE (Y(5),THH)
      EQUIVALENCE (Y(6),THHD)
      EQUIVALENCE (Y(7),P)
      EQUIVALENCE (Y(8),HDHT)
      EQUIVALENCE (Y(9),YW)
      EQUIVALENCE (Y(10),FCONT)
      EQUIVALENCE (Y(11),FINPUT)
      EQUIVALENCE (Y(12),EKIN)
      EQUIVALENCE (Y(13),EPOT)
      EQUIVALENCE (Y(14),ENERGY)
      EQUIVALENCE (Y(15),F1OUT)
      EQUIVALENCE (Y(16),F2OUT)
      EQUIVALENCE (Y(17),HDOUT)
      EQUIVALENCE (Y(18),RINOUT)
```

```
      IF (NEWDT) 100,300,200
*****************************************************************

C              ******  FIRST TIMESTEP ONLY  ******
100   CONTINUE

C
C   State Variables and Their Time Derivatives:
C
   !    TH1     theta_1          (lower link rotation)
   !    TH2     theta_2          (upper link rotation)
   !    THH     theta_H          (head rotation)
   !    P       cylinder presssure
   !    TH1D    theta_1-dot
   !    TH2D    theta_2-dot
   !    THHD    theta_H-dot
   !    PD      derivative of cylinder pressure
   !    TH1DD   theta_1-double-dot
   !    TH2DD   theta_2-double-dot
   !    THHDD   theta_H-double-dot
C
C   Auxiliary variables:
C
   !    THE     theta_E          (elbow link position)
   !    THED    theta_E_dot
   !    TE      elbow torque from spring and damper
   !    HDHT    height of the end of the head link (apex frame)
   !    YW      wire height
   !    FCONT   contact force
   !    EKIN    kinetic energy
   !    EPOT    potential energy
   !    ENERGY  total system energy
   !    PDOWN   downstream pressure
   !    PUP     upstream pressure
   !    FPDPU   a function of upstream and downstream pressures
   !    FINPUT  applied air cylinder force
   !    YFRAME  height of frame at the datum bar
C
C   Input parameters:
C
110   FORMAT(F20.0)
130   FORMAT(I2)
   ! dimensions
      READ (8,110) L1          !lower link length (m)
      READ (8,110) L2          !upper link length (m)
      READ (8,110) LH          !head frame length (m)
      READ (8,110) D1          !distance to lower link c-of-m (m)
      READ (8,110) D2          !distance to upper link c-of-m (m)
      READ (8,110) DH          !distance to head c-of-m (m)
   ! masses
      READ (8,110) M1          !lower link mass (kg)
```

```
      READ (8,110) M2          !upper link mass (kg)
      READ (8,110) MH          !head mass (kg)
! moments of inertia
      READ (8,110) I1          !lower link moment of inertia (kg-m^2)
      READ (8,110) I2          !upper link moment of inertia (kg-m^2)
      READ (8,110) IH          !head moment of inertia (kg-m^2)
! springs
      READ (8,110) KS          !input (catenary) spring rate (N/m)
      READ (8,110) KH          !head spring rate (N-m/rad)
! coulomb frictions
      READ (8,110) BC1         !base coulomb friction (N-m)
      READ (8,110) BC2         !knuckle coulomb friction (N-m)
      READ (8,110) BCH         !head coulomb friction (N-m)
! viscous damping
      READ (8,110) BV1         !base viscous damping (N-sec)
      READ (8,110) BV2         !knuckle viscous damping (N-sec)
      READ (8,110) BVH         !head viscous damping (N-sec)
! elbow linkage
      READ (8,110) KE          !elbow stiffness (N/m)
      READ (8,110) XF          !x-coordinate of the base link (m)
      READ (8,110) YF          !y-coordinate of the base link (m)
      READ (8,110) LE          !length of the elbow link (m)
      READ (8,110) THE0        !initial value of THE (at TH1=0) (rad)
      PI=3.14159
      TRMA=(L1-XF)**2-LE**2
      TRMB=-2.0*(L1-XF)*YF
      TRMC=YF**2-LE**2
      PH1=ATAN2(-TRMB-SQRT(TRMB**2-4.0*TRMA*TRMC),2.0*TRMA)
      XG=L1+LE*COS(PH1-PI/2.0)
      YG=LE*SIN(PH1-PI/2.0)
      DFG0=SQRT((XG-XF)**2+(YG+YF)**2)
                               !calculated initial 4th bar length (m)
! air cylinder data
      READ (8,110) RGAS        !universal gas constant (m^2/sec^2-K)
      READ (8,110) TEMP        !cylinder temperature (K)
      READ (8,110) GRAV        !gravitational acceleration (m/sec^2)
      READ (8,110) CD          !discharge coefficient (dimensionless)
      READ (8,110) GAMMA       !specific heat ratio (dimensionless)
      READ (8,110) PATM        !atmospheric pressure (N/m^2)
      READ (8,110) PSUPPG      !supply gauge pressure (N/m^2)
      PSUPP=PSUPPG+PATM        !supply absolute pressure (N/m^2)
! air cylinder dimensions
      READ (8,110) AREA        !piston surface area (m^2)
      READ (8,110) AO          !orifice area (m^2)
      READ (8,110) CYLVOL0     !volume when (ALFA-TH1)=PI/2 (m^3)
      READ (8,110) LMARM       !moment arm length for cylinder (m)
      READ (8,110) ALFA        !angle, lower link to moment arm (rad)
! linear suspension parameters
      READ (8,110) KCYL        !simple cylinder spring (N/m)
      READ (8,110) BVCYL       !simple cylinder damper (N-sec/m)
      READ (8,130) NCYL        !choice of cylinder models (0=linear)
```

```
   ! catenary parameters:
        READ (5,110) CYCLES      !sinusoidal input frequency (Hz)
        READ (5,110) AMPL        !sinusoidal input amplitude (m)
        READ (8,110) OPHT        !operating wire height (m)
        FREQ=CYCLES*2.0*PI       !input frequency (rad/sec)
   ! plotting offsets
        READ (8,110) OFF1        !ram input curve offset
        READ (8,110) OFF2        !head link curve offset
        READ (8,110) OFF3        !upper link curve offset
        READ (8,110) OFF4        !lower link curve offset
C
C   Initial Conditions:
C
        READ (8,110) TH1         !TH1 initial condition
        READ (8,110) TH2         !TH2 initial condition
        READ (8,110) THH         !THH initial condition
c       SINTH=(OPHT+AMPL)/(2.0*L1)
c       TH1=ASIN(SINTH)
c       TH2=TH1
c       THH=0.0
        YW=OPHT

        IF (NCYL.EQ.0) THEN
        P=LMARM*COS(ALFA-TH1)
        ELSE
        P=PSUPP
        ENDIF
C
C   Define some useful constants:
C
        GASCNS=CD*AO*SQRT(2.0*GAMMA*RGAS*TEMP/(GAMMA-1.0))

        AK1=I1+M1*D1**2+M2*L1**2+MH*L1**2
        BK1=M2*L1*D2+MH*L1*L2
        CK1=MH*L1*DH
        DK1=M2*L1*D2+MH*L1*L2
        DK2=MH*L1*DH
        DK3=KS*L1
        DK4=M1*GRAV*D1+M2*GRAV*L1+MH*GRAV*L1
        DK5=KS*L1**2
        DK6=KS*L1*L2
        DK7=KS*L1*LH
        EK1=M2*L1*D2+MH*L1*L2
        FK1=I2+M2*D2**2+MH*L2**2
        GK1=MH*L2*DH
        HK1=M2*L1*D2+MH*L1*L2
        HK2=MH*L2*DH
        HK3=KS*L2
        HK4=M2*GRAV*D2+MH*GRAV*L2
        HK5=KS*L2**2
        HK6=KS*L1*L2
```

```
      HK7=KS*L2*LH
      IK1=MH*L1*DH
      JK1=MH*L2*DH
      KK1=IH+MH*DH**2
      LK1=MH*L1*DH
      LK2=MH*L2*DH
      LK3=KS*LH
      LK4=MH*GRAV*DH
      LK5=KS*LH**2
      LK6=KS*L1*LH
      LK7=KS*L2*LH

**********************************************************************

C              ******  BETWEEN TIMESTEPS  ******
200   CONTINUE
C
C   Recalculate abbreviations.
C
      S1=SIN(TH1)
      C1=COS(TH1)

      S2=SIN(TH2)
      C2=COS(TH2)

      SH=SIN(THH)
      CH=COS(THH)
C
C   For energy check, recalculate THE.
C
      LC1MXF=L1*C1-XF
      LS1PYF=L1*S1+YF
      TRMA=LC1MXF**2-LE**2
      TRMB=-2.0*LC1MXF*LS1PYF
      TRMC=LS1PYF**2-LE**2
      SRD=SQRT(TRMB**2-4.0*TRMA*TRMC)
      PH1=ATAN2(-TRMB-SRD,2.0*TRMA)
      XG=L1*C1+LE*SIN(PH1)
      YG=L1*S1-LE*COS(PH1)
      DFG=SQRT((XG-XF)**2+(YG+YF)**2)
      THE=THE0+(DFG-DFG0)/LE-TH1
C
C   Calculate (old) auxiliary variables for output.
C
      HDHT=L1*S1+L2*S2+LH*SH
      FCONT=KS*(HDHT-YW)
      YFRAME=L1*S1+L2*S2
C
C   Energy calculation:
C
      X2D=-L1*TH1D*S1+D2*TH2D*S2
```

```
      Y2D=L1*TH1D*C1+D2*TH2D*C2
      XHD=-L1*TH1D*S1+L2*TH2D*S2-DH*THHD*SH
      YHD=L1*TH1D*C1+L2*TH2D*C2+DH*THHD*CH
      EKIN=.5*((I1+M1*D1**2)*TH1D**2
     1          +I2*TH2D**2+M2*(X2D**2+Y2D**2)
     2          +IH*THHD**2+MH*(XHD**2+YHD**2))
      YS=HDHT
      Y1=D1*S1
      Y2=L1*S1+D2*S2
      YH=L1*S1+L2*S2+DH*SH
      EPOT=.5*(KH*THH**2+KS*(YW-YS)**2)
     1          +GRAV*(M1*Y1+M2*Y2+MH*YH)
     2     +.5*KE*(TH2-THE)**2
C
C   For energy to balance, set damping and inputs to zero.
C
      ENERGY=EKIN+EPOT
C
C   Output data-like states.
C
      F1OUT=L1*S1-OPHT/2.0+OFF4
      F2OUT=L2*S2-OPHT/2.0+OFF3
      HDOUT=LH*SH+OFF2
      RINOUT=YW-OPHT+OFF1
C
C   At each timestep, output the plotted states to a file.
C
      IF (T.GT.2.0) THEN
      WRITE (9,677)RINOUT,HDOUT,F2OUT,F1OUT
677   FORMAT (4(3X,F10.7))
      ELSE
      CONTINUE
      ENDIF
C
C   Calculate the height of the (sinusoidal) catenary.
C   This defines the new contact force.
C
      YW=OPHT+AMPL*(1.0-COS(FREQ*T))
C
C   Define some useful quantities.
C
      DY3=YW*DK3
      HY3=YW*HK3
      LY3=YW*LK3
*****************************************************************

C              ******  DURING TIMESTEPS  ******
300   CONTINUE
      IF (NCYL.EQ.0) GOTO 310
C
C   Determine up-stream and down-stream pressures.
```

```
C
      IF (P.GT.PSUPP) THEN
            PUP=P
            PDOWN=PSUPP
      ELSE
            PUP=PSUPP
            PDOWN=P
      ENDIF

      CYLVOL=CYLVOL0+AREA*LMARM*COS(ALFA-TH1)
      CYLVOLD=AREA*TH1D*SIN(ALFA-TH1)

      PDPU=PDOWN/PUP
      PD=GASCNS/CYLVOL*PUP*(PDPU)**(1.0/GAMMA)
     &    *SQRT(1.0-PDPU**(GAMMA-1.0/GAMMA))
     &    -P*CYLVOLD/CYLVOL
      FINPUT=(P-PATM)*AREA
      GOTO 320
C
C   Simple (linear) cylinder equations.
C
310   XCYL=LMARM*COS(ALFA-TH1)-P
      PD=KCYL*XCYL/BVCYL
      FINPUT=PSUPPG*AREA-KCYL*XCYL
320   CONTINUE
C
C   Abbreviations:
C
      S1=SIN(TH1)
      C1=COS(TH1)

      S2=SIN(TH2)
      C2=COS(TH2)

      SH=SIN(THH)
      CH=COS(THH)

      S12=SIN(TH1+TH2)
      C12=COS(TH1+TH2)

      S2H=SIN(TH2+THH)
      C2H=COS(TH2+THH)

      S1H=SIN(TH1-THH)
      C1H=COS(TH1-THH)

      SH1=SIN(THH-TH1)
C
C   Calculate the elbow link position and the elbow torque.
C
      LC1MXF=L1*C1-XF
```

```
      LS1PYF=L1*S1+YF
      TRMA=LC1MXF**2-LE**2
      TRMB=-2.0*LC1MXF*LS1PYF
      TRMC=LS1PYF**2-LE**2
      SRD=SQRT(TRMB**2-4.0*TRMA*TRMC)
      PH1=ATAN2(-TRMB-SRD,2.0*TRMA)
      XG=L1*C1+LE*SIN(PH1)
      YG=L1*S1-LE*COS(PH1)
      DFG=SQRT((XG-XF)**2+(YG+YF)**2)
      THE=THE0+(DFG-DFG0)/LE-TH1
C
C   Calculate DTHEDTH1.
C
      DCDTH1=2.0*LS1PYF*L1*C1
      DBDTH1=-2.0*(LC1MXF*L1*C1-LS1PYF*L1*S1)
      DADTH1=-2.0*LC1MXF*L1*S1
      DPH1DTH1=(-TRMA**2/(2.0*TRMA**2+TRMB**2-
     1          2.0*TRMA*TRMC+TRMB*SRD))*
     2          (DBDTH1/TRMA-TRMB*DADTH1/TRMA**2+
     3          (TRMB*DBDTH1-2.0*(TRMA*DCDTH1+
     4          TRMC*DADTH1))/(TRMA*SRD)-
     5          SRD*DADTH1/TRMA**2)
      DYGDTH1=L1*C1+LE*SIN(PH1)*DPH1DTH1
      DXGDTH1=-L1*S1+LE*COS(PH1)*DPH1DTH1
      DFGDTH1=((XG-XF)*DXGDTH1+(YG+YF)*DYGDTH1)
     &        /SQRT((XG-XF)**2+(YG+YF)**2)
      DTHEDTH1=DFGDTH1/LE-1.0
C
C   The equations of motion are as follows:
C              A*TH1DD + B*TH2DD + C*THHDD = D
C              E*TH1DD + F*TH2DD + G*THHDD = H
C              I*TH1DD + J*TH2DD + K*THHDD = L
C   where A,B,C,D,E,F,G,H,I,J,K,L are functions of the three
C   rotational state variables, their first time derivatives,
C   the state variable P, the input YW, and the system parameters.
C
      A=AK1
      B=BK1*C12
      C=CK1*C1H
      D=TH2D**2*S12*DK1
     1  +THHD**2*SH1*DK2
     2  +C1*(DY3-DK4)
     3  -S1*C1*DK5-C1*S2*DK6-C1*SH*DK7
     4  +FINPUT*LMARM*SIN(ALFA-TH1)-KE*(THE-TH2)*DTHEDTH1
     5  -SIGN(BC1,TH1D)-SIGN(BC2,TH1D+TH2D)
     6  -BV1*TH1D-BV2*(TH1D+TH2D)

      E=EK1*C12
      F=FK1
      G=GK1*C2H
      H=TH1D**2*HK1*S12
```

```
     1    +THHD**2*HK2*S2H
     2    +C2*(HY3-HK4)
     3    -S2*C2*HK5-S1*C2*HK6-C2*SH*HK7
     4    -KE*(TH2-THE)
     5    -SIGN(BC2,TH1D+TH2D)-SIGN(BCH,TH2D+THHD)
     6    -BV2*(TH1D+TH2D)-BVH*(TH2D+THHD)

          I=IK1*C1H
          J=JK1*C2H
          K=KK1
          L=TH1D**2*LK1*S1H
     1     +TH2D**2*LK2*S2H
     2     +CH*(LY3-LK4)
     3     -SH*CH*LK5-S1*CH*LK6-S2*CH*LK7
     4     -THH*KH-SIGN(BCH,TH2D+THHD)
     5     -BVH*(TH2D+THHD)

C
C    Define some abbreviations.
C
          FAEB=F*A-E*B
          GAEC=G*A-E*C
          HAED=H*A-E*D
          JAIB=J*A-I*B
          KAIC=K*A-I*C
          LAID=L*A-I*D
C
C    Equations to be integrated:
C
          THHDD=(FAEB*LAID-JAIB*HAED)/(FAEB*KAIC-JAIB*GAEC)
          TH2DD=(HAED-GAEC*THHDD)/FAEB
          TH1DD=(D-B*TH2DD-C*THHDD)/A
C
C    Derivitives of state variables:
C
          FY(1)=TH1D
          FY(2)=TH1DD
          FY(3)=TH2D
          FY(4)=TH2DD
          FY(5)=THHD
          FY(6)=THHDD
          FY(7)=PD

          RETURN
          END
```